Scattering from Cavity-Backed Apertures: The Generalized Dual Series Solution of the Concentrically Loaded *E*-Pol Slit Cylinder Problem

RICHARD W. ZIOLKOWSKI AND J. BRIAN GRANT

Abstract—**The generalized dual series solution to the scattering of an *E*-polarized (*E*-pol) plane wave from an infinite circular cylinder having an infinite axial slot and enclosing an infinite concentric impedance cylinder is presented. This solution explicitly exhibits the correct edge behavior, and it can handle cylinders that are either electrically small or large without special considerations. The angle of incidence is arbitrary. A variety of current, field, and cross-section results are presented. These are compared with the corresponding *H*-pol problem results to establish the polarization dependencies of the aperture coupling. It is also shown that effects corresponding to the presence of the interior cavity dominate all of the scattering data. In particular, the bistatic cross sections in either case and the current induced along an interior wire in the *E*-pol case exhibit new resonance features that are due to the cavity-backed nature of the aperture.**

I. Introduction

BECAUSE THEY DESCRIBE coupling via apertures into enclosed regions *and* scattering from reflector structures having edges and nontrivial geometries, the importance of canonical electromagnetic cavity-backed aperture problems cannot be overstated. They provide a fundamental means with which basic aperture coupling and reflector physics can be studied in detail; they can be used to construct and/or validate approximate models or general engineering analysis and design "rules of thumb" that can be applied to more general apertures and scattering objects; and they aid in the development of improved numerical techniques especially near the edges of the apertures or reflectors where discontinuities appear and where those methods may encounter difficulties. Moreover, accurate canonical solutions of this type provide standards to which general numerical code results can be compared.

In this paper, we construct the generalized dual series solution to the scattering of an *E*-polarized plane wave from an infinite circular cylinder having an infinite axial slot and enclosing an infinite concentric impedance cylinder. The generalized dual series (GDS) approach was introduced in [1] to solve mixed boundary problems of the electromagnetic aperture coupling type and was applied directly in [2] and [3] to the corresponding empty and concentrically loaded *H*-polarized slit cylinder problems. The empty *E*-pol slit cylinder problem has received some attention in the literature with various techniques. It was investigated with an integral equation approach by Senior [4] and with approximate analytical approaches by Libelo and his coworkers (see for instance [5]). Shestopalov and his coworkers in the Soviet Union have examined this problem with limiting cases of its dual series solution (see for instance [6]); Warne has constructed a uniform approximation of its dual series solution valid for small apertures [7]. This paper represents an extension of the results reported in [8].

As will be shown in Section II, the GDS approach is systematic. One first constructs the modal expansions of the fields in the interior and in the exterior regions. Then the electromagnetic boundary conditions: $E_{\tan} = 0$ over the metal and $H_{\tan}$ continuous in the aperture, are enforced. This leads to a dual series problem for the modal coefficients. For a two-dimensional scattering problem of this type, the resultant dual series problem is solved by transforming it into an equivalent Riemann–Hilbert problem. The solution to a Riemann–Hilbert problem of complex variable theory is well known [9] and for these aperture coupling problems, returns an infinite linear system of equations for the modal coefficients. A rigorous truncation procedure for this system was developed in [2]. The resulting finite system can be solved for the solution coefficients with a variety of techniques such as Gauss elimination.

In principle the currents, fields, etc. can be generated from the original expansions with these solution coefficients. However, because we are dealing with modal expansions, purely numerical summations do not faithfully reproduce the singularities present in the currents and in the fields. As discussed in Section III, the asymptotic behavior of the solution coefficients can be identified and is used to produce analytically summed series that recover the singular behavior of those physical quantities near the edge of the aperture. Thus by "preconditioning" the current and field sums with these analytical components, the remaining sums are well-behaved and may be handled numerically without difficulty.

Manuscript received March 25, 1986; revised August 25, 1986. This work was supported by the U.S. Department of Energy under Contract W-7405-ENG-48.

The authors are with the Engineering Research Division, Lawrence Livermore National Laboratory, P.O. Box 5504, L-156, Livermore, CA 94550.

IEEE Log Number 8613180.

As such, the GDS approach allows one to obtain essentially analytical solutions to a large family of canonical aperture coupling problems. By a variation of a single parameter, the impedance, the slit cylinder can be empty or made to enclose a perfectly conducting or lossy wire. The computer is utilized only in the final stages of the solution process to generate the special functions, to perform the matrix inversion and to calculate the numerical sums. The GDS solution inherently contains the behavior near the rim of the aperture required by Meixner's edge conditions, and it can handle slit cylinders that are either electrically small or large without additional special considerations. The angle of incidence is arbitrary. Typical E-pol current, field, and cross-section results will be described in detail in Section IV. These will be compared with the corresponding H-pol results to examine the polarization dependencies of the aperture coupling and the scattering data. It will be shown that effects corresponding to the presence of the interior cavity dominate all of the results. In particular, we will demonstrate that the bistatic cross sections in either case and the current induced along an interior wire in the E-pol case exhibit new resonance features that are due to the cavity-backed nature of the aperture.

II. Generalized Dual Series Solution

A. Problem Geometry

The E-pol problem configuration is shown in Fig. 1(a). A cylindrical coordinate system (r, ϕ, z) is erected at the common centers of the slit and impedance cylinders with the z-axis along their axes. The radius of the impedance cylinder is a; the slit cylinder radius is b. The extent of the metal is taken to be the interval $[\Theta, 2\pi - \Theta]$, the aperture is $[-\Theta, \Theta]$. The plane wave is incident from the angle ϕ^{inc}.

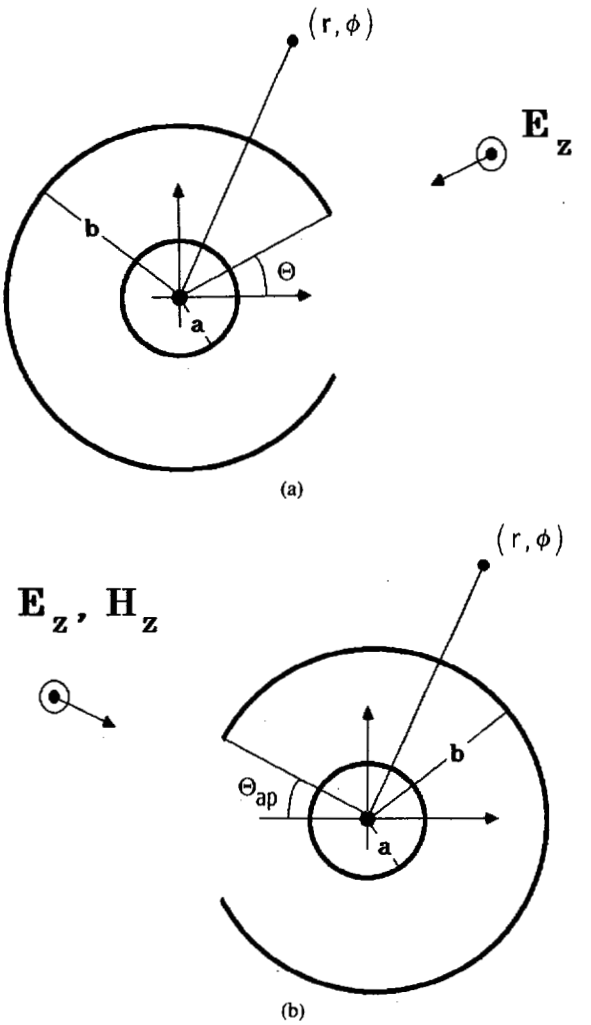

Fig. 1. (a) Configuration of the scattering of an E-pol plane wave from an infinite cylinder having an infinite axial slot and enclosing a concentric impedance surface. (b) Configuration for the comparisons of the E-pol and H-pol problem results.

B. Modal Expansions of the Fields

Fourier mode decompositions of the incident and scattered fields are readily constructed. For an E-polarized incident plane wave of amplitude E_0 the electric field is along the axes of the cylinders and has the expansion for $r > b$

$$E_z^{inc} = e^{jkr\cos(\phi-\phi^{inc})} = E_0 \sum_{m=-\infty}^{\infty} j^{|m|} J_{|m|}(kr) e^{jm(\phi-\phi^{inc})}. \tag{1a}$$

An $e^{j\omega t}$ time dependence is assumed and supressed throughout. The resulting magnetic field components for $r > b$ have the form

$$H_r^{inc} = \frac{j}{\omega\mu_0 r}\partial_\phi E_z^{inc} = \frac{-Y_0}{r} E_0 \sum_{m=-\infty}^{\infty} m j^{|m|} J_{|m|}(kr) e^{jm(\phi-\phi^{inc})} \tag{1b}$$

$$H_\phi^{inc} = \frac{-j}{\omega\mu_0}\partial_r E_z^{inc} = -jY_0 E_0 \sum_{m=-\infty}^{\infty} j^{|m|} J'_{|m|}(kr) e^{jm(\phi-\phi^{inc})}. \tag{1c}$$

The corresponding scattered field expansions are assumed to be

$$E_z^s = E_0 \sum_{m=-\infty}^{\infty} e^{jm\phi} \cdot \begin{cases} [B_m J_{|m|}(kr) + C_m H_{|m|}(kr)], & (a<r<b) \\ A_m H_{|m|}(kr), & (r>b) \end{cases} \tag{2}$$

$$H_r^s = \frac{-Y_0}{r} E_0 \sum_{m=-\infty}^{\infty} e^{jm\phi} m \cdot \begin{cases} [B_m J_{|m|}(kr) + C_m H_{|m|}(kr)], & (a<r<b) \\ A_m H_{|m|}(kr), & (r>b) \end{cases} \tag{3a}$$

$$H_\phi^s = -jY_0 E_0 \sum_{m=-\infty}^{\infty} e^{jm\phi} \cdot \begin{cases} [B_m J'_{|m|}(kr) + C_m H'_{|m|}(kr)], & (a<r<b) \\ A_m H'_{|m|}(kr), & (r>b) \end{cases} \tag{3b}$$

where Y_0 is the free space admittance ($Y_0 Z_0 = 1$) and where

H_m represents the Hankel function of order m and of the second kind.

The number of coefficients is reduced by applying the impedance boundary condition on the inner cylinder and by enforcing E_z to be continuous across the outer cylinder $r = b$. The impedance boundary condition

$$E_z^{\text{tot}}(a, \phi) = ZH_\phi^{\text{tot}}(a, \phi)$$

produces the coefficient relation

$$C_m = \Omega_{|m|}(ka)B_m \tag{4a}$$

where

$$\Omega_{|m|}(ka) = -\left[\frac{jZ_0 J_{|m|}(ka) - ZJ'_{|m|}(ka)}{jZ_0 H_{|m|}(ka) - ZH'_{|m|}(ka)}\right]. \tag{4b}$$

Enforcing the continuity of E_z^{tot} across $r = b$ gives

$$A_m = B_m \frac{\alpha_{|m|}(kb)}{H_{|m|}(kb)} - j^{|m|}\frac{J_{|m|}(kb)}{H_{|m|}(kb)} e^{-jm\phi^{\text{inc}}} \tag{5a}$$

where

$$\alpha_{|m|}(kr) = J_{|m|}(kr) + \Omega_{|m|}(ka)H_{|m|}(kr). \tag{5b}$$

Combining these relations, the total field expressions in terms of the unknown coefficients B_m become finally

$$E_z^{\text{tot}} = E_0 \sum_{m=-\infty}^{\infty} e^{jm\phi} B_m \alpha_{|m|}(kr), \qquad (a < r < b) \tag{6a}$$

$$E_z^{\text{tot}} = E_0 \sum_{m=-\infty}^{\infty} e^{jm\phi} \left\{ B_m \frac{\alpha_{|m|}(kb)H_{|m|}(kr)}{H_{|m|}(kb)} + j^{|m|}e^{-jm\phi^{\text{inc}}} \cdot \left[\frac{J_{|m|}(kr)H_{|m|}(kb) - J_{|m|}(kb)H_{|m|}(kr)}{H_{|m|}(kb)}\right]\right\}, \qquad (r > b)$$

$$H_r^{\text{tot}} = \frac{-Y_0}{r} E_0 \sum_{m=-\infty}^{\infty} e^{jm\phi} mB_m \alpha_{|m|}(kr), \qquad (a < r < b) \tag{6b}$$

$$H_r^{\text{tot}} = \frac{-Y_0}{r} E_0 \sum_{m=-\infty}^{\infty} \cdot e^{jm\phi} m \left\{ B_m \frac{\alpha_{|m|}(kb)H_{|m|}(kr)}{H_{|m|}(kb)} + j^{|m|}e^{-jm\phi^{\text{inc}}} \cdot \left[\frac{J_{|m|}(kr)H_{|m|}(kb) - J_{|m|}(kb)H'_{|m|}(kr)}{H_{|m|}(kb)}\right]\right\}, \qquad (r > b)$$

$$H_\phi^{\text{tot}} = -jY_0 E_0 \sum_{m=-\infty}^{\infty} e^{jm\phi} B_m \alpha'_{|m|}(kr), \qquad (a < r < b) \tag{6c}$$

$$H_\phi^{\text{tot}} = -jY_0 E_0 \sum_{m=-\infty}^{\infty} e^{jm\phi} \left\{ B_m \frac{\alpha_{|m|}(kb)H'_{|m|}(kr)}{H_{|m|}(kb)} + j^{|m|}e^{-jm\phi^{\text{inc}}} \cdot \left[\frac{J'_{|m|}(kr)H_{|m|}(kb) - J_{|m|}(kb)H'_{|m|}(kr)}{H_{|m|}(kb)}\right]\right\}, \qquad (r > b).$$

C. Equivalent Dual Series Problem and Its Solution

The dual series problem is constructed by enforcing the remaining electromagnetic boundary conditions: $E_z^{\text{tot}} = 0$ over the metal and H_ϕ^{tot} continuous in the aperture. With (6) evaluated at $r = b$ and with the Wronskian relation

$$J_{|m|}(kb)H'_{|m|}(kb) - J'_{|m|}(kb)H_{|m|}(kb) = -\frac{2j}{\pi kb}$$

one obtains the metal equation:

$$\sum_{m=-\infty}^{\infty} B_m \alpha_{|m|}(kb)e^{jm\phi} = 0, \qquad (|\phi| > \Theta) \tag{7a}$$

and the aperture equation:

$$\sum_{m=-\infty}^{\infty} \frac{B_m}{H_{|m|}(kb)} e^{jm\phi} = \sum_{m=-\infty}^{\infty} \frac{j^{|m|}e^{-jm\phi^{\text{inc}}}}{H_{|m|}(kb)} e^{jm\phi}, \qquad (|\phi| < \Theta). \tag{7b}$$

The dual series system defined by (7a) and (7b) has a form slightly different from the ones treated in [2] and in [3]. However, with a redefinition of terms, one can put the present system into the desired form. In particular, let

$$b_m = B_m \alpha_{|m|}(kb) \tag{8a}$$

$$\tau_m = \frac{1}{-j\pi\alpha_{|m|}(kb)H_{|m|}(kb).} \tag{8b}$$

and

$$f(\phi) = \sum_{m=-\infty}^{\infty} f_m e^{jm\phi} \tag{8c}$$

where

$$f_m = \frac{j^{|m|}e^{-jm\phi^{\text{inc}}}}{-j\pi H_{|m|}(kb)}. \tag{8d}$$

Then (7) becomes

$$\sum_{m=-\infty}^{\infty} b_m e^{jm\phi} = 0, \qquad (|\phi| > \Theta) \tag{9a}$$

$$\sum_{m=-\infty}^{\infty} b_m \tau_m e^{jm\phi} = f(\phi), \qquad (|\phi| < \Theta). \tag{9b}$$

This dual series system can now be solved with the approach developed in [1].

We proceed by introducing the functions χ_m so that

$$\tau_m = \begin{cases} -\xi, & \text{for } m = 0 \\ |m|(1 + \chi_m), & \text{for } m \neq 0. \end{cases} \tag{10}$$

As shown in Appendix I, in the static limit, $kb \ll 1$, χ_m is a constant for each m and goes to zero as $(a/b)^{2|m|}$ for m large. Moreover, χ_m behaves like $(kb/m)^2$ for large m; i.e., for

finite kb: $\lim_{m\to\infty} \chi_m \sim O(|m|^{-2})$. Thus $\tau_m \sim |m|$ for $kb \ll 1$ or for $m \to \infty$.

The dual series equations are then rewritten as

$$\sum_{m=-\infty}^{\infty} b_m e^{jm\phi} = 0, \qquad (|\phi| > \Theta) \tag{11a}$$

$$\sum_{m=-\infty}^{\infty} b_m |m| e^{jm\phi} = \xi b_0 + f_0 + \sum_{n\neq 0} (f_n - |n|\chi_n b_n) e^{jn\phi}, \qquad (|\phi| < \Theta). \tag{11b}$$

The terms proportional to χ_m have been moved to the right-hand side because for large m they are of order $|m|^{-2}$ smaller than the corresponding terms remaining on the left-hand side of (11b). We have, therefore, isolated the large m pieces on the left-hand side of the dual series equations (11). These terms are responsible for the edge behavior. The terms proportional to χ_m are now treated as forcing terms and are negligible when $(kb/m)^2$ is small or when $kb \ll 1$ and m is large. Since in the quasistatic limit τ_m in (9) reduces to $|m|$ plus a piece that is effectively included with f as a forcing term, we denote (11) the "static" dual series problem. Note that this identification is exact when $a = 0$. Thus the solution of the "static" dual series system (11) will contain all of the information about the edge behavior of the "nonstatic" or dynamic problem. This attribute of the static problem is generally recognized. The "static" dual series system (11) with the right-hand side treated as a general forcing function can be solved exactly by converting it to a Riemann–Hilbert problem.

The Riemann–Hilbert problem is a classical problem in complex variable theory. It concerns the construction of the analytic function x whose limits x_+ and x_- from the inside and the outside of a closed curve satisfy the transition condition $x_- = gx_+ + h$ on an open segment of that curve.

Recall that (7a) and (7b) are, respectively, associated with the field components E_z and H_ϕ. Therefore, they behave, respectively, like $(\Theta - \phi)^{+1/2}$ and $(\Theta - \phi)^{-1/2}$ near the edge of the aperture. Consequently, (9a) and (9b), hence (11a) and (11b), inherit this behavior. The additional term $|m|$ in (11b) is responsible for this difference. To make both series equations express the same singular behavior, (11a) is differentiated with respect to ϕ. Introducing the coefficients $x_m = mb_m$ (note that it is assumed that $x_0 \equiv 0$) and the functions

$$x_+(z) = \sum_{m>0} x_m z^m$$

$$x_-(z) = -\sum_{m<0} x_m z^m \equiv \sum_{m>0} x_m z^{-m}$$

$$F(z) = \xi b_0 + \sum_{m=-\infty}^{\infty} \left(f_m - x_m \frac{|m|}{m}\chi_m\right) z^m,$$

the dual series (11) can then be written simply as

$$x_+(e^{j\phi}) - x_-(e^{j\phi}) = 0, \qquad (|\phi| > \Theta) \tag{12a}$$

$$x_+(e^{j\phi}) + x_-(e^{j\phi}) = F(e^{j\phi}), \qquad (|\phi| < \Theta). \tag{12b}$$

This system represents the equivalent Riemann–Hilbert problem. Equation (12a) reflects the continuity of the electric field across the metal; (12b), the transition condition the magnetic field must satisfy across the aperture to compensate for the absense of any current there. A Riemann–Hilbert problem of this form has both a bounded and an unbounded solution that are intrinsically endowed with a square root behavior near $\phi = \Theta$. [9, sec. 42, pp. 420–428]. Recognizing that our procedure has embedded a square root singularity into (12), we select the unbounded solution. The GDS solution we obtain then inherently contains the edge behavior required by Meixner's conditions.

Introducing the coefficients

$$F_m = f_m - x_m \frac{|m|}{m}\chi_m$$

the Riemann–Hilbert problem solution is [1]

$$x_m = \xi b_0 V_m^0 + \sum_{n=-\infty}^{\infty} F_n V_m^n + x_{-1} P_m \tag{13a}$$

where ($m = 0, \pm 1, \pm 2, \cdots$) and P_m denotes the Legendre polynomial of order m. Unless otherwise indicated, the argument of any Legendre polynomial is cos Θ. These coefficient relations must be completed with the auxiliary condition

$$b_0 = -\sum_{m\neq 0} \frac{(-)^m}{m} x_m$$

which is obtained from (11a) with $\phi = \pi$; it is introduced to account for the constant eliminated in the differentiation that led from (11a) to (12a). This constraint leads to the coefficient expression

$$-b_0 = \xi b_0 W^0 + \sum_{n=-\infty}^{\infty} F_n W^n + 2Sx_{-1} \tag{13b}$$

where

$$W^n = \sum_{m\neq 0} \frac{(-)^m}{m} V_m^n \quad \text{and} \quad S = \frac{1}{2}\sum_{m\neq 0} \frac{(-)^m}{m} P_m. \tag{14}$$

The coefficients V_m^n, W^0, W^n, and S are all simply combinations of Legendre's polynomials P_m (cos Θ) and are given in Appendix II. Equations (13a) and (13b) uniquely define the "static" solution modal coefficients.

The relations defining the nonstatic solution coefficients are obtained from the static system by reintroducing the explicit expressions for the terms F_n which contain the unknown coefficients x_n. This yields an infinite linear system of equations:

$$x_m = \xi b_0 V_m^0 + \sum_{n=-\infty}^{\infty} V_m^n \left(f_n - \frac{|n|}{n}\chi_n x_n\right) + x_{-1} P_m \tag{15a}$$

$$-b_0 = \xi b_0 W^0 + \sum_{n=-\infty}^{\infty} W^n \left(f_n - \frac{|n|}{n}\chi_n x_n\right) + 2Sx_{-1}, \tag{15b}$$

where ($m = 0, \pm 1, \pm 2, \cdots$), which uniquely defines the desired modal coefficients.

D. Numerical Implementation

The solution system (15) is an infinite set of equations of the form:

$$x_m + \sum_{n=-\infty}^{\infty} \Lambda_{mn} x_n = \sum_{n=-\infty}^{\infty} \Gamma_{mn} f_n$$

$$b_0 = \sum_{n=-\infty}^{\infty} \sum_{m\neq 0} \frac{(-)^m}{m} \Lambda_{mn} x_n - \sum_{n=-\infty}^{\infty} \sum_{m\neq 0} \frac{(-)^m}{m} \Gamma_{mn} f_n.$$

Because its operator form is $y + Ly = G$, where y is a vector representing the infinitely many unknowns, this infinite linear system can be interpreted from a Hilbert space point of view as a Fredholm equation of the second kind [10]. It can be treated in several ways. The approach developed by Johnson and Ziolkowski [2] is systematic and has proved to be very efficient. Because Λ_{mn} and f_n rapidly approach zero for large values of n, truncation of Λ_{mn} for $|n|$ greater than some value N can be justified rigorously. Typically, reasonable convergence is achieved with $N \sim 10kb$. This truncation eliminates x_n in the sums for $|n| > N$. Solving by Gauss elimination (or some similar technique) the remaining $2N + 1$ by $2N + 1$ square system of linear equations:

$$x_m + \sum_{n=-N}^{N} \Lambda_{mn} x_n = \sum_{n=-N}^{N} \Gamma_{mn} f_n \tag{16a}$$

$$b_0 = \sum_{n=-N}^{N} \mathrm{L}_n x_n - \sum_{n=-N}^{N} G_n f_n \tag{16b}$$

where

$$\mathrm{L}_n \equiv \sum_{m\neq 0} \frac{(-)^m}{m} \Lambda_{mn},\ G_n \equiv \sum_{m\neq 0} \frac{(-)^m}{m} \Gamma_{mn} \tag{16c}$$

and where $m = -N, -N + 1, \cdots, +N$ yields good numerical approximations for the coefficients $b_0, x_{\pm 1}, \cdots, x_{\pm N}$. Additional coefficients x_m for $M \geq |m| > N$ are easily and accurately generated directly from (16a). As N approaches infinity, this approximate scheme becomes exact.

III. Calculation of the Observables

The electric and magnetic fields everywhere, the currents induced on the slit cylinder and on an interior conducting cylinder, and the bistatic cross sections may be readily computed from their modal expansions once the solution coefficients b_0 and $b_m = x_m/m$ ($m \neq 0$) are known. However, alternate expressions are particularly useful in increasing the rate of convergence of the current and field sums and in studying their behavior near the edge of the aperture. They are described below. They are constructed by introducing an asymptotic (large m) form of the solution coefficients x_m:

$$\tilde{x}_m = \kappa_1 P_m + \kappa_2 P_{m+1} \tag{17}$$

and a slight variation of it:

$$\tilde{x}_m = \kappa_1 P_m + \kappa_2 \frac{m}{m+1} P_{m+1}, \qquad \text{for } m > 0$$

$$\tilde{x}_{-m} = \kappa_1 \frac{m}{m-1} P_{m-1} + \kappa_2 \frac{m}{m-2} P_{m-2}, \qquad \text{for } m > 0,\ m \neq 1, 2 \tag{17'}$$

where the terms

$$\kappa_1 = \frac{1}{2}\left[\xi b_0 P_1 + \sum_{n=-N}^{N} F_n P_{n+1} + 2x_{-1}\right] \tag{18a}$$

$$\kappa_2 = -\frac{1}{2}\left[\xi b_0 + \sum_{n=-N}^{N} F_n P_n\right]. \tag{18b}$$

To obtain (17), for instance, we have taken in the truncated form of (13a) an asymptotic form of the coefficients V_m^n:

$$\tilde{V}_m^n = \frac{1}{2}\left[P_{n+1} P_m - P_n P_{m+1}\right]$$

so that

$$\tilde{x}_m = \xi b_0 \tilde{V}_m^0 + \sum_{n=-N}^{N} F_n \tilde{V}_m^n + x_{-1} P_m \equiv \kappa_1 P_m + \kappa_2 P_{m+1}.$$

The need for two asymptotic forms of the solution coefficients arises from a basic difference between the current (on the slit cylinder) and H_ϕ sums and the E_z and H_r sums which reflects the difference in the behavior between these terms near the edge of the aperture.

A. Slit Cylinder Current Sums

The current on the slit cylinder is simply the difference between the scattered magnetic fields on its interior and exterior. Explicitly, it is axially directed and is defined by

$$\begin{aligned} J_z &= H_{\phi>}(kb, \phi) - H_{\phi<}(kb, \phi) \\ &= -\frac{2Y_0 E_0}{\pi kb} \sum_{m=-\infty}^{\infty} e^{jm\phi} \left[\frac{B_m}{H_{|m|}(kb)} - \frac{j^{|m|} e^{-jm\phi^{\mathrm{inc}}}}{H_{|m|}(kb)}\right] \\ &= +\frac{2jY_0 E_0}{kb} \left[b_0 \tau_0 - f(\phi) + J_s(\phi)\right] \end{aligned} \tag{19}$$

where the sum

$$J_s(\phi) = \sum_{m\neq 0} b_m \tau_m e^{jm\phi} = \sum_{m\neq 0} \frac{x_m \tau_m}{m} e^{jm\phi}. \tag{20}$$

This sum is preconditioned by introducing the asymptotic forms of the solution coefficients x_m and of the coefficients τ_m given by (17), $\tilde{x}_m$, and $|m|$, respectively:

$$J_s(\phi) = \tilde{J}_s + \sum_{m\neq 0} \left(\frac{x_m \tau_m - \tilde{x}_m |m|}{m}\right) e^{jm\phi} \tag{21}$$

where the asymptotic sum

$$\tilde{J}_s(\phi)=\sum_{m\neq 0}\frac{\tilde{x}_m\tau_{|m|}}{m}e^{jm\phi} \tag{22}$$

can be calculated analytically. As shown in Appendix III, the expression

$$\tilde{J}_s(\phi)=-2je^{-j\phi}\left[\frac{\kappa_1 e^{j\phi/2}+\kappa_2 e^{-j\phi/2}}{\sqrt{2(\cos\Theta-\cos\phi)}}-j\kappa_2\right]$$
$$-(\kappa_1+\kappa_2\cos\Theta) \tag{22'}$$

is obtained in a straightforward manner. It contains the square root singularity of the current near the edge of the aperture; i.e., for $\phi\sim\Theta-\epsilon$ which gives $\cos\phi\sim\cos\Theta+\epsilon\sin\Theta$, the term

$$[2(\cos\phi-\cos\Theta)]^{-1/2}\sim\epsilon^{-1/2}.$$

The first sum in (19), $f(\phi)$, converges rapidly because $(1/H_{|m|}(kb))\sim|m|^{-|m|}$ as $|m|\to\infty$. The second sum in (21) also converges rapidly numerically. Both of those sums are truncated for $|m|>M$.

B. Electric and Magnetic Field Sums

The electric and magnetic field sums are preconditioned in a similar manner. The resultant expressions for the components of the total (incident + scattered) fields in terms of the dual series solution coefficients are

$$\frac{E_z^{\text{tot}}}{E_0}=\sum_{l=0}^{2}b_l\frac{\alpha_l(kr)}{\alpha_l(kb)}e^{-jl\phi}$$
$$+\sum_{m=1}^{\infty}e^{jm\phi}\left[\frac{x_m}{m}\frac{\alpha_m(kr)}{\alpha_m(kb)}-\frac{\tilde{x}_m}{m}\left(\frac{r}{b}\right)^m\right]$$
$$-\sum_{m=3}^{\infty}e^{-jm\phi}\left[\frac{x_{-m}}{m}\frac{\alpha_m(kr)}{\alpha_m(kb)}-\frac{\tilde{x}_{-m}}{m}\left(\frac{r}{b}\right)^m\right]$$
$$+S_z(r/b,\phi),\qquad(a<r<b) \tag{23a}$$

$$\frac{E_z^{\text{tot}}}{E_0}=\sum_{m=-\infty}^{\infty}e^{jm(\phi-\phi^{\text{inc}})}j^{|m|}$$
$$\cdot\left[\frac{J_{|m|}(kr)H_{|m|}(kb)-J_{|m|}(kb)H_{|m|}(kr)}{H_{|m|}(kb)}\right]$$
$$+\sum_{l=0}^{2}b_l\frac{H_l(kr)}{H_l(kb)}e^{-jl\phi}$$
$$+\sum_{m=1}^{\infty}e^{jm\phi}\left[\frac{x_m}{m}\frac{H_m(kr)}{H_m(kb)}-\frac{\tilde{x}_m}{m}\left(\frac{b}{r}\right)^m\right]$$
$$-\sum_{m=3}^{\infty}e^{-jm\phi}\left[\frac{x_{-m}}{m}\frac{H_m(kr)}{H_m(kb)}-\frac{\tilde{x}_{-m}}{m}\left(\frac{b}{r}\right)^m\right]$$
$$+S_z(b/r,\phi),\qquad(r>b)$$

$$\frac{H_r^{\text{tot}}}{E_0}=\frac{-Y_0}{r}\left\{\sum_{m\neq 0}e^{jm\phi}\left[x_m\frac{\alpha_{|m|}(kr)}{\alpha_{|m|}(kb)}-\tilde{x}_m\left(\frac{r}{b}\right)^{|m|}\right]\right.$$
$$\left.+S_r(r/b,\phi)\right\},\qquad(a<r<b) \tag{23b}$$

$$\frac{H_r^{\text{tot}}}{E_0}=\frac{-Y_0}{r}\left\{\sum_{m=-\infty}^{\infty}e^{jm(\phi-\phi^{\text{inc}})}mj^{|m|}\right.$$
$$\cdot\left[\frac{J_{|m|}(kr)H_{|m|}(kb)-J_{|m|}(kb)H_{|m|}(kr)}{H_{|m|}(kb)}\right]$$
$$+\sum_{m\neq 0}e^{jm\phi}\left[x_m\frac{H_{|m|}(kr)}{H_{|m|}(kb)}-\tilde{x}_m\left(\frac{b}{r}\right)^m\right]$$
$$\left.+S_r(b/r,\phi)\right\},\qquad(r>b).$$

$$\frac{H_\phi^{\text{tot}}}{E_0}=-jY_0\left\{\sum_{m\neq 0}e^{jm\phi}\left[\frac{x_m}{m}\frac{\alpha'_{|m|}(kr)}{\alpha'_{|m|}(kb)}\right.\right.$$
$$\left.-\operatorname{sgn}(m)\frac{\tilde{x}_m}{kr}\left(\frac{r}{b}\right)^{|m|}\right]$$
$$\left.+\left(\frac{1}{kr}\right)S_\phi(r/b,\phi)\right\},\qquad(a<r<b) \tag{23c}$$

$$\frac{H_\phi^{\text{tot}}}{E_0}=-jY_0\left\{\sum_{m=-\infty}^{\infty}e^{jm(\phi-\phi^{\text{inc}})}j^{|m|}\right.$$
$$\cdot\left[\frac{J'_{|m|}(kr)H_{|m|}(kb)-J_{|m|}(kb)H'_{|m|}(kr)}{H_{|m|}(kb)}\right]$$
$$+\sum_{m\neq 0}e^{jm\phi}\left[\frac{x_m}{m}\frac{H'_{|m|}(kr)}{H_{|m|}(kb)}-\operatorname{sgn}(m)\frac{\tilde{x}_m}{kr}\left(\frac{b}{r}\right)^{|m|}\right]$$
$$\left.+\left(\frac{1}{kr}\right)S_\phi(b/r,\phi)\right\},\qquad(r>b),$$

where $\operatorname{sgn}(m)=+1$ for $m>0$, -1 for $m<0$. As shown in Appendix IV, identifying the quantities

$$\lambda_+=\lambda e^{j\phi}$$
$$\lambda_-=\lambda e^{-j\phi}$$

so that $|\lambda_+|<1$ and $|\lambda_-|<1$ and introducing the terms:

$$K(\lambda)=\ln\left(\frac{2}{1-\cos\Theta\lambda+\sqrt{1-2\lambda\cos\Theta+\lambda^2}}\right) \tag{24}$$

$$L(\lambda)=\frac{1}{\sqrt{1-2\lambda\cos\Theta+\lambda^2}}, \tag{25}$$

the analytically calculated sums are

$$S_z(\lambda, \phi) = (\kappa_1 + \lambda_+^{-1}\kappa_2)K(\lambda_+) - \lambda_-(\kappa_1 + \lambda_-\kappa_2)K(\lambda_-) + (\kappa_1\lambda_-^2 - \kappa_2)\cos\Theta \quad (26a)$$

$$S_r(\lambda, \phi) = (\kappa_1 + \lambda_+^{-1}\kappa_2)L(\lambda_+) + \lambda_-(\kappa_1 + \lambda_-\kappa_2)L(\lambda_-) - (\kappa_1 + \kappa_2\cos\Theta) - \kappa_2\lambda_+^{-1}(1 - \lambda_+\lambda_-) \quad (26b)$$

$$S_\phi(\lambda, \phi) = (\kappa_1 + \lambda_+^{-1}\kappa_2)L(\lambda_+) - \lambda_-(\kappa_1 + \lambda_-\kappa_2)L(\lambda_-) - (\kappa_1 + \kappa_2\cos\Theta) - \kappa_2\lambda_+^{-1}(1 + \lambda_+\lambda_-). \quad (26c)$$

Note that for $r = b$ the factors $\lambda_+ = e^{j\phi}$ and $\lambda_- = e^{-j\phi}$ so that near the edge of the aperture where $\phi \sim \Theta - \epsilon$, the field terms

$$(1 - 2\lambda_+\cos\Theta + \lambda_+^2)^{-1/2} = e^{-j\phi/2}[2(\cos\phi - \cos\Theta)]^{-1/2} \sim \epsilon^{-1/2}$$

$$(1 - 2\lambda_-\cos\Theta + \lambda_-^2)^{-1/2} = e^{+j\phi/2}[2(\cos\phi - \cos\Theta)]^{-1/2} \sim \epsilon^{-1/2}.$$

This demonstrates that the square root singularities of the transverse field components H_r and H_ϕ near the aperture edge have been isolated in the S_r and S_ϕ expressions, hence, are treated analytically. The summations in (23a)–(23c) are handled numerically without difficulty and converge rapidly.

C. Current on an Interior Wire

A basic quantity of great interest in electromagnetic pulse (EMP) studies and in other aperture coupling applications is the total current induced on an interior wire. It is a measure of how well a particular field that has penetrated into the interior of an object through an aperture has coupled to an interior load. For the present two-dimensional configuration the total current per unit length along the wire is defined by the integral relation:

$$I_z = a\int_0^{2\pi} H_\phi(a, \phi)\, d\phi.$$

Because (6c) for H_ϕ is in the form of a Fourier expansion, this expression reduces to one which depends only on the solution coefficient b_0:

$$I_z = -jY_0E_0(2\pi a)b_0\frac{\alpha_0'(ka)}{\alpha_0'(kb)}. \quad (27)$$

D. Bistatic Cross Section

A basic quantity of great interest in scattering studies is the bistatic cross section. It allows one to sample the magnitude of the scattered far-field pattern at any desired look angle. For an E-polarized scattering problem in two dimensions it is defined as

$$\sigma_{BS}(\phi, \phi^{\text{inc}}) = \lim_{r\to\infty} 2\pi r\frac{|E_z^{\text{scat}}(r, \phi)|^2}{|E_z^{\text{inc}}(r, \phi^{\text{inc}})|^2}.$$

With the $r > b$ expression in (2) and (5a) and (8a) this simply becomes

$$\sigma_{BS}(\phi, \phi^{\text{inc}}) = \frac{4}{k}\left|\sum_{m=-\infty}^{\infty}\frac{j^{|m|}e^{jm\phi}}{H_{|m|}(kb)}\cdot[b_m - j^{|m|}e^{-jm\phi^{\text{inc}}}J_{|m|}(kb)]\right|^2 \approx \frac{4}{k}\left|\sum_{-M}^{M}\frac{j^{|m|}e^{jm\phi}}{H_{|m|}(kb)}[b_m - j^{|m|}e^{-jm\phi^{\text{inc}}}J_{|m|}(kb)]\right|^2. \quad (28)$$

IV. Numerical Results

Typical results generated by the E-pol generalized dual series solution are given below and are compared with those generated by the corresponding H-pol solution. These will include currents induced on the slit cylinder and on an interior wire, electric fields, and cross sections. The E-pol results are all calculated with the expressions derived in Section III. The corresponding H-pol results utilize analogous relations, most of which are derived in [2] and [3]. The electric field results are all presented as contour plots of $|E_{\text{total}}|/|E_{\text{inc}}(r = 0)|$. To make the E- and H-pol comparisons more effective, our E-pol field plots will be referenced to the configuration natural for the H-pol case. This H-pol geometry is given in Fig. 1(b) and simply has the slit cylinder rotated by 180° with respect to the one shown in Fig. 1(a). All angles will now be referred to this geometry so that, for example, a plane wave incident from 180.0° (0.0°) sees (does not see) the aperture. The angle ϕ^{inc} is denoted by ϕ_0 on all of the plots. Half of the angular extent of the aperture is denoted by the angle Θ_{ap}. All of these results will be used to illustrate some general characteristics of the coupling physics and of scattering from cavity-backed apertures that our studies of these canonical problems have revealed.

The real and imaginary parts and the magnitude of the axial current $-J_z$ induced on an empty slit cylinder of radius 1.0 λ with $\Theta = 90°$, or equivalently, $\Theta_{\text{ap}} = 90°$ by an E-pol plane wave incident at 180° and at 90° are shown, respectively, in Figs. 2(a) and 2(b). These plots can be compared directly to the corresponding H-polarized results given by [2, figs. 3 and 4]. In contrast to the square root to zero behavior of the H-pol currents, the E-pol currents display the square root singularity near the edge of the aperture required by Meixner's edge conditions. The number of peaks in the magnitude of the current in the normal incidence case (Fig. 2(a)) closely corresponds to the length of the cylinder's perimeter which is 3.14 λ. The current in Fig. 2(b) is skewed toward the lit region as one might expect for this nonnormal incidence case.

The utility of these canonical solutions for studying the near-fields of a cylindrical reflector antenna with varying sized blockages is illustrated with Fig. 3. The E-pol electric fields $E^{\text{tot}} = E_z$ are shown for a 1.0 λ semicylinder ($\Theta_{\text{ap}} = 90°$) reflector at normal incidence ($\phi^{\text{inc}} = 180°$), (a) without any blockage and with wire blockages of radii (b) 0.1 λ, (c) 0.3 λ, and (d) 0.5 λ. Focusing is apparent in Fig. 3(a). Noticable perturbations from Fig. 3(a) are found in the field patterns on

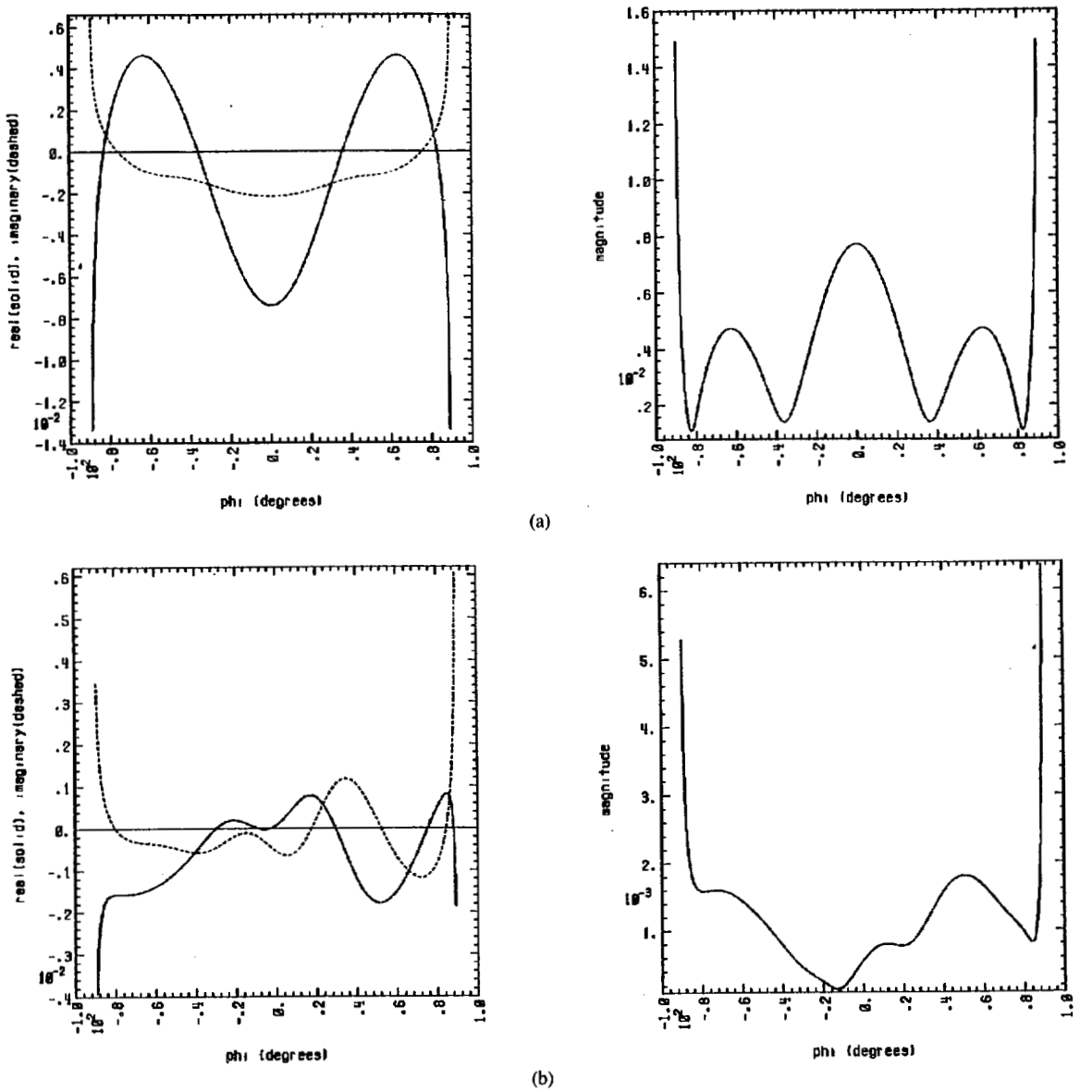

Fig. 2. The GDS solution produces the required square root singularities of the slit cylinder current near the edge of the aperture as shown by the real and imaginary parts and the magnitude of J_z induced on an empty slit cylinder, $b = 1.0\,\lambda$ and $\Theta_{ap} = 90°$, by an E-pol plane wave incident from (a) 180° and (b) 90°.

the source side of the blockages while well-defined modal patterns become established in the waveguide channel formed between the wires and the reflector in Figs. 3(b)–3(d). The transitions from the three well-defined field peaks in Figs. 3(b) and 3(c) to the "banana" mode in Fig. 3(d) is accompanied by a significant enhancement of the local field strengths. Notice that there is a close correspondence between the location of the field maximums near the reflector in Fig. 3(a) and the current peaks in Fig. 2(a).

Fig. 4 represents a quasistatic E-pol coupling example in which a slit cylinder of radius $b = 0.1\,\lambda$ is (a) empty and (b) is loaded with an interior wire of radius $a = 0.1\,b$. The plane wave is normally incident and $2\Theta_{ap} = 28.6°$. The penetration is minimal as expected. Moreover, there is very little difference between the empty, Fig. 4(a), and the loaded cylinder, Fig. 4(b), cases. On the other hand, the corresponding large kb case, where $b/\lambda = 10.0$ or $kb = 62.8$, is shown in Fig. 5. It demonstrates that the penetration level into the interior of the slit cylinder can be quite high. There is approximately only a three-fold enhancement of the field in the empty cylinder case, Fig. 5(a), and a twenty-two fold enhancement in the loaded cylinder case, Fig. 5(b). The locations of the maximum field values in the loaded cylinder case lie on the shadow boundary of the wire at the points $(x, y) = (0.1, \pm 0.1)$. This is due to the form of the particular pattern that is established in the interior of the cylinder. Note that the geometrical optics shadow boundary of the slit cylinder, where the field ratio is 0.5, is readily apparent in both figures.

One of the important features of coupling through a cavity-

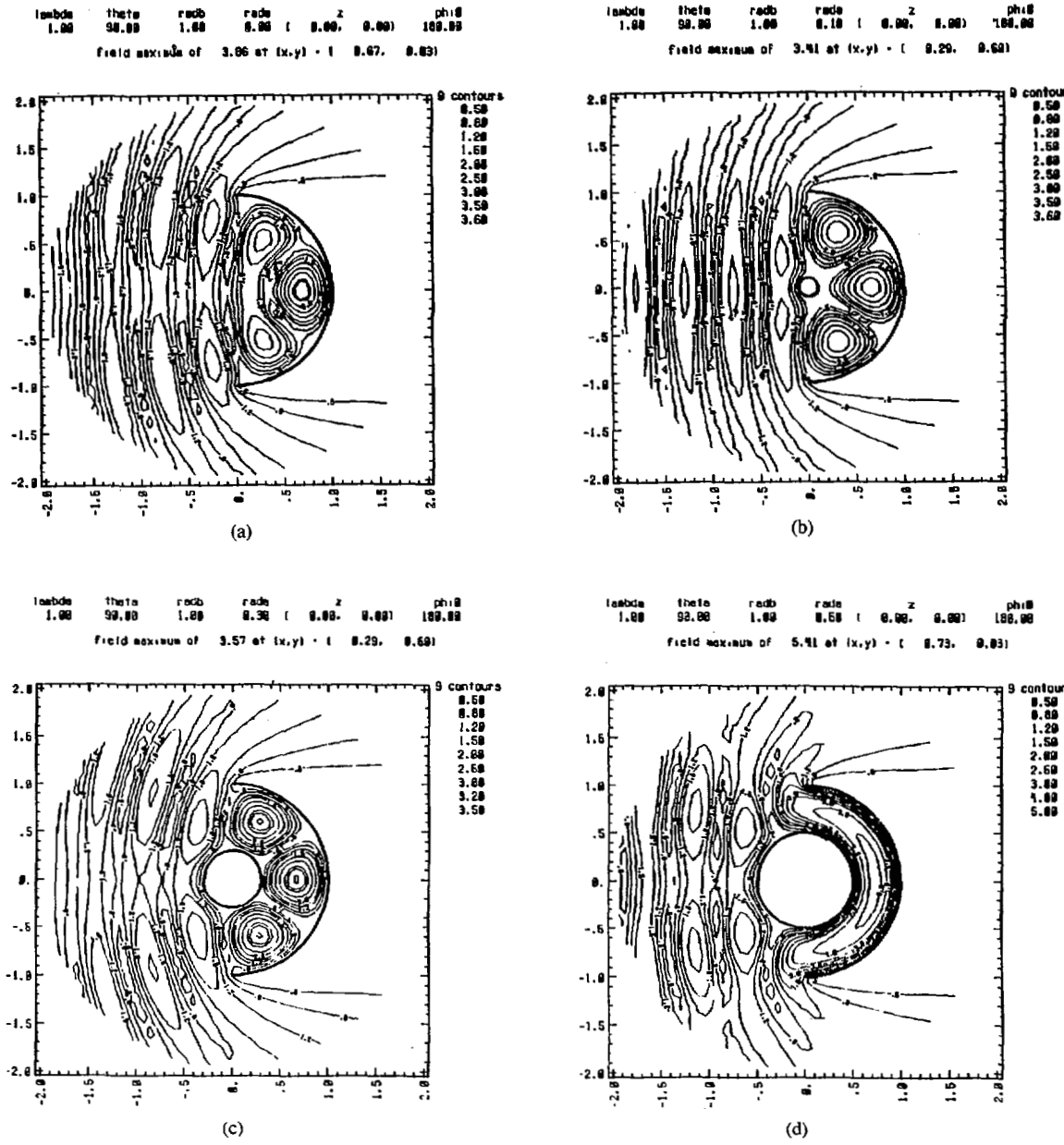

Fig. 3. The GDS solution can be used to study the effects of blockage near a reflector as shown by contour plots of the electric field generated by an E-pol plane wave incident from 180° upon a slit cylinder, $b = 1.0\ \lambda$ and $\Theta_{ap} = 90.0°$, when (a) it is empty and when it encloses a wire of radius (b) 0.1 λ, (c) 0.3 λ, and (d) 0.5 λ.

backed aperture that has been verified with the E- and H-pol dual series solutions is that the field patterns in the interior of the open cavity are closely related to those of the natural modes of the corresponding closed cavity. Consider Fig. 6. An E-pol plane wave is normally incident from 180° on a slit cylinder of radius $b = 1.0$ m having a 2° aperture ($\Theta_{ap} = 1.0°$). The wavelength of the incident field is chosen to match that of one of the TM circular waveguide modes [11, p. 205]. In Figs. 6(a), 6(b), 6(c), and 6(d) the wavelength is, respectively, 1.138 m, 1.640 m, 0.7465 m, and 1.2235 m corresponding to the TM_{02}, TM_{11}, TM_{22}, and TM_{21} waveguide modes. The recovery of the field patterns characteristic of those waveguide modes is unmistakable. The interesting point is that these modal features persist even for relatively large apertures. Moreover, the coupling of the field into the interior of the cylinder is large and occurs despite the aperture being small and/or nonresonant (i.e., the length of the aperture is not an integer multiple of a half-wavelength). In Fig. 7 the aperture of the cylinder with $b = 1.0$ m has been increased to 28.6° ($\Theta_{ap} = 14.3°$). This particular choice of Θ_{ap} makes the aperture a half-wavelength long when $\lambda = 1.0$ m. Fig. 7(a) shows the empty cylinder results for $\lambda = 1.183$ m. The corresponding loaded cylinder case is given in Fig. 7(b). Both figures indicate a significant amount of coupling into the

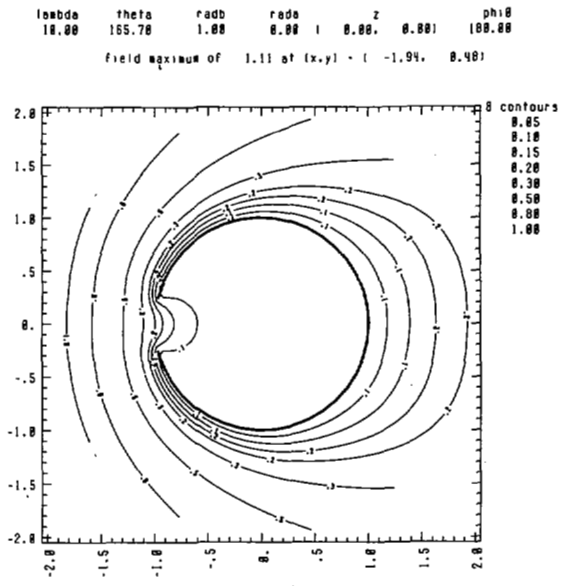

(a)

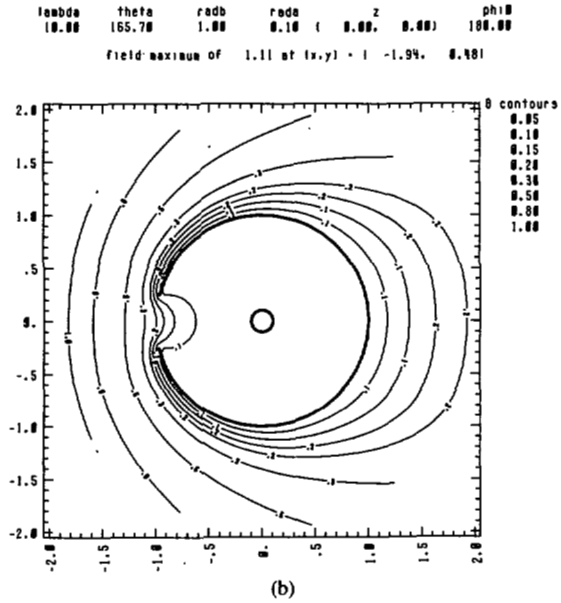

(b)

Fig. 4. The efficacy of the GDS approach in quasistatic cases is illustrated with contour plots of the electric field generated by an E-pol plane wave incident from 180° upon a slit cylinder, $b = 0.1\,\lambda$ and $2\Theta_{ap} = 28.6°$, when (a) it is empty, and (b) it encloses a wire with $a = 0.01\,\lambda$.

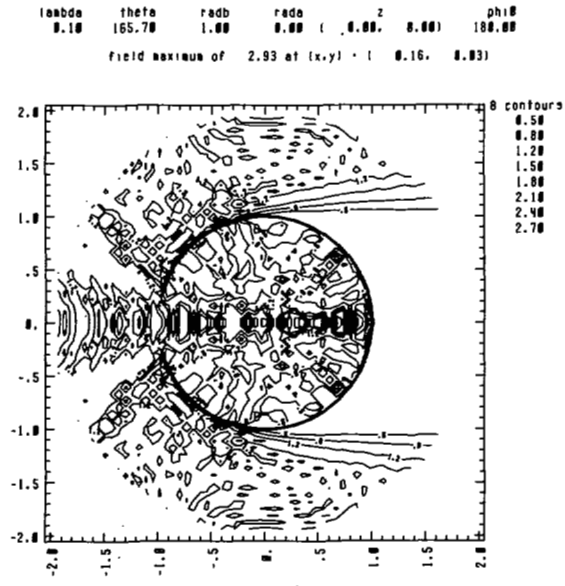

(a)

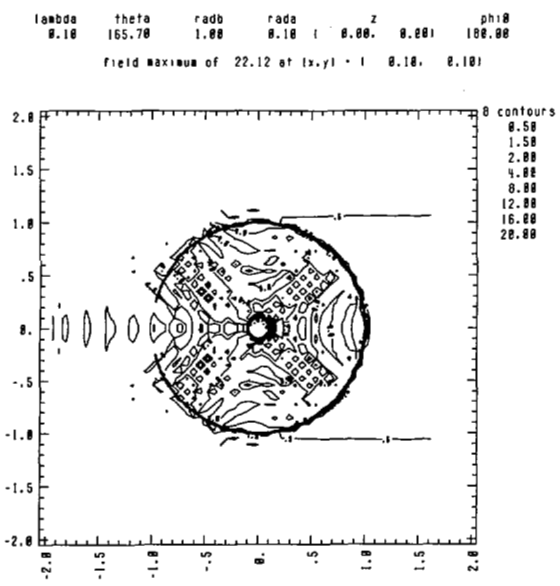

(b)

Fig. 5. The efficacy of the GDS approach when the scatterer is many wavelengths in size is illustrated with contour plots of the electric field generated by an E-pol plane wave incident from 180° upon a slit cylinder, $b = 10.0\,\lambda$ and $2\Theta_{ap} = 28.6°$, when (a) it is empty, and (b) it encloses a wire with $a = 1.0\,\lambda$.

interior. The TM_{02} pattern persists in Fig. 7(a). The presence of the interior wire in Fig. 7(b) has driven the pattern into a coax TM_{21} form and the location of the maximum field strength out of the cylinder to a point directly in front of the aperture. Increasing the aperture extent further to 90° results in the patterns shown in Fig. 8. Although they are beginning to degrade slightly, the TM_{02} and the coax TM_{21} patterns are still dominant in Figs. 8(a) and 8(b), respectively. A difference between Figs. 7(b) and 8(b) that is particularly noticeable is the region of maximum field strength, which has been translated to an interior point directly in front of the wire.

The closed waveguide patterns also persist as the angle of incidence is varied. The major effect is a general decrease in the interior field strengths. This is illustrated in Fig. 9. The E-pol plane wave is incident from 180° in Fig. 9(a); 135° in Fig. 9(b). The slit cylinder again has an aperture of 28.6° ($\Theta_{ap} = 14.3°$). The TM_{31} mode is excited in both cases. The maximum field amplitude in Fig. 9(a) is 1.5 times the one in Fig. 9(b).

As the radius of the interior wire is increased, the standard waveguide modes are no longer appropriate and new modal patterns develop. This is illustrated in Fig. 10 for an E-pol plane wave with $\lambda = 1.0$ m that is incident upon a cylinder of

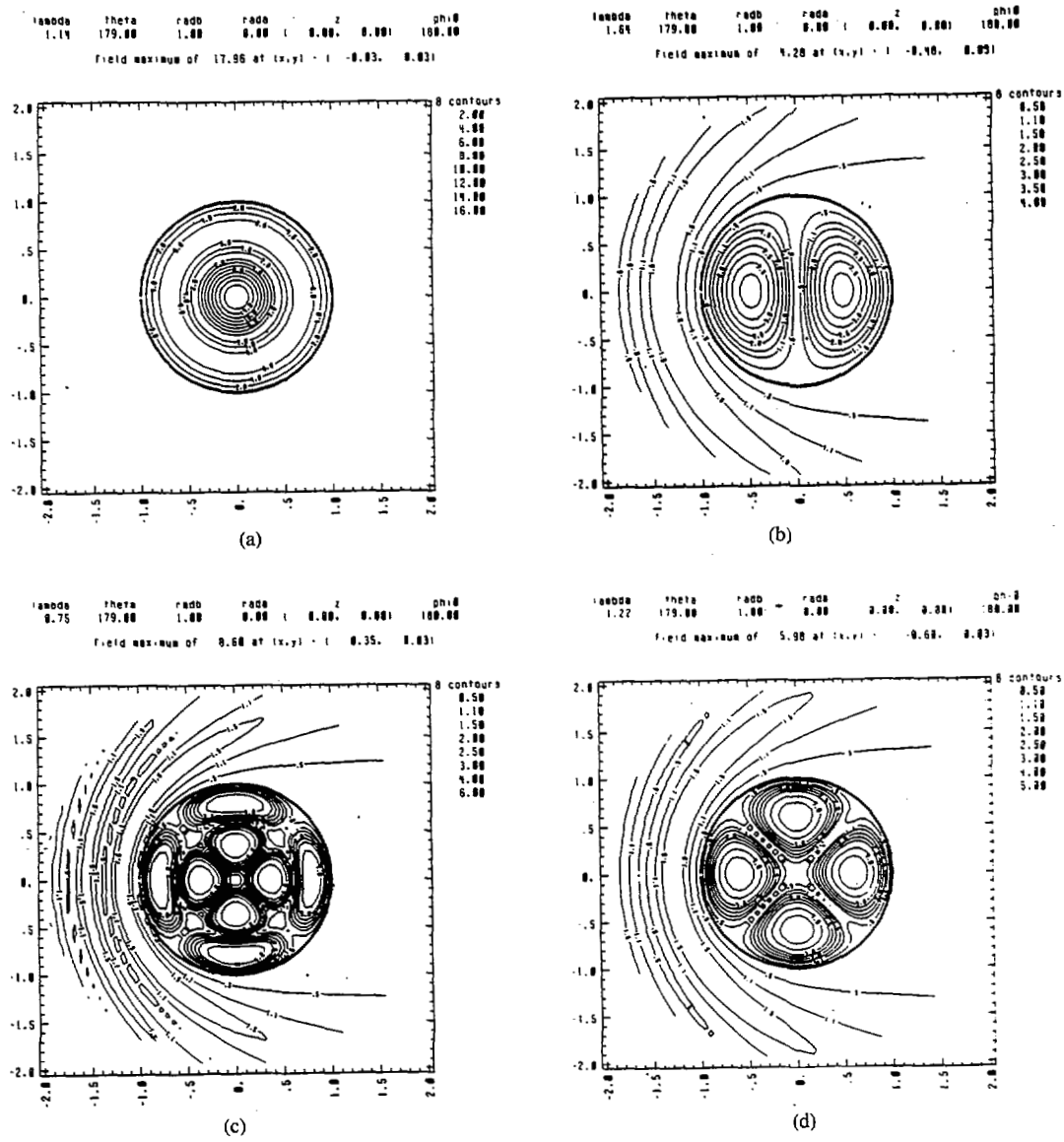

Fig. 6. Coupling to the closed waveguide modes is demonstrated with contour plots of the electric field generated by an E-pol plane wave incident from 180° upon an empty slit cylinder, $b = 1.0$ m and $2\Theta_{ap} = 2°$, when the wavelength (a) $\lambda = 1.138$ m, (b) $\lambda = 1.640$ m, (c) $\lambda = 0.7465$ m, (d) $\lambda = 1.2235$ m.

radius $b = 1.0$ m enclosing an interior wire of radius $a = 0.5$ m. It is incident from 180° in Fig. 10(a); 135° in Fig. 10(b). The "banana" mode pattern met in Fig. 3(d) for the open reflector structure is again formed in this cavity-backed aperture case but with a very substantial increase in its maximum directly behind the wire. There is about a twelve-fold enhancement of the field in the normally incident case, Fig. 10(a), which decreases to only a fourfold enhancement in the not normally incident case, Fig. 10(b).

A large increase in the radius of the interior wire can actually result in the exclusion of the field from the interior cavity. This is illustrated in Fig. 11. An E-pol plane wave is normally incident from 180.0° with $\lambda = 1.183$ m upon a slit cylinder of radius $b = 1.0$ m having a 28.6° ($\Theta_{ap} = 14.3°$) aperture. In Fig. 7(a), which is repeated in Fig. 11(a), the slit cylinder encloses a wire of radius $a = 0.1$ m. The field has penetrated into the interior and has excited the coax TM_{21} mode. In contrast, the wire radius is $a = 0.5$ m in Fig. 11(b) and the field has not penetrated deeply into the interior. However, the field maximum now occurs just behind the aperture and represents an enhancement of 4.05 rather than 2.35. Fig. 11(b) shows that the incident field has a wavelength that is below cut-off for the wire/slit cylinder waveguide, hence, does not penetrate into the interior cavity.

To view the effects of polarization on these coupling results, consider Figs. 12–15. In Figs. 12 and 13 a plane wave is incident from 180° on a slit with $b = 1.0\ \lambda$ and $\Theta_{ap} = 45°$. The E-pol cases are illustrated in Figs. 12(a) and 13(a); the H-pol cases in Figs. 12(b) and 13(b). The slit cylinder is empty for Figs. 12(a) and 12(b); it encloses a wire of radius $a = 0.1$

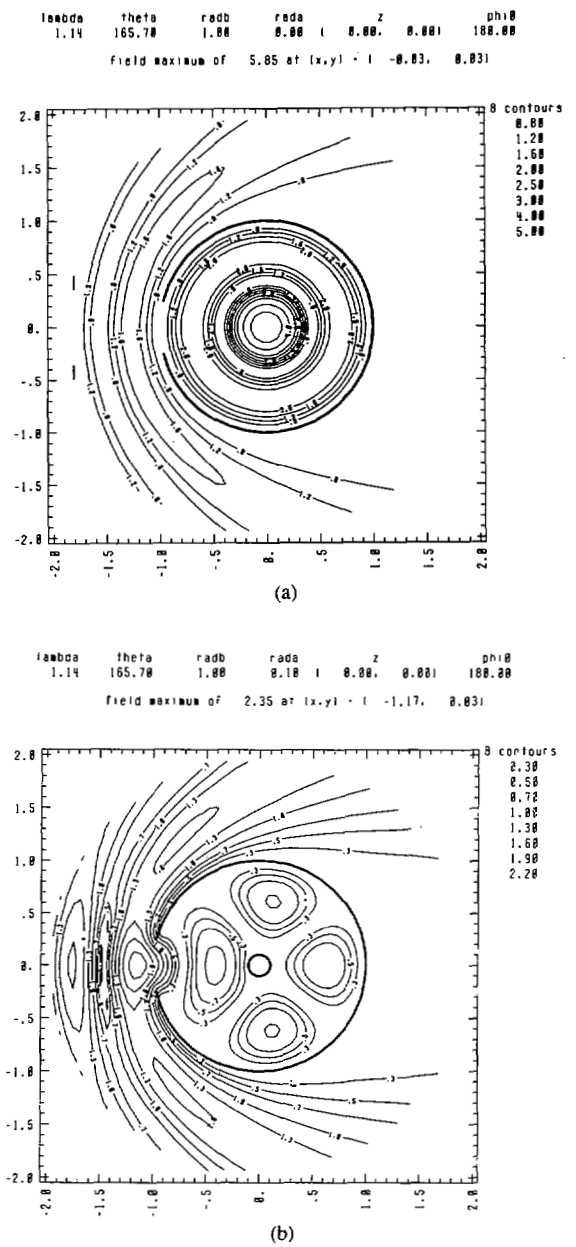

Fig. 7. The persistence of the cavity modes when the aperture is large is shown by contour plots of the electric field generated by an E-pol plane wave with $\lambda = 1.138$ m incident from 180° upon a slit cylinder, $b = 1.0$ m and $2\Theta_{ap} = 28.6°$, when (a) it is empty, and (b) it encloses a wire with $a = 0.1$ m.

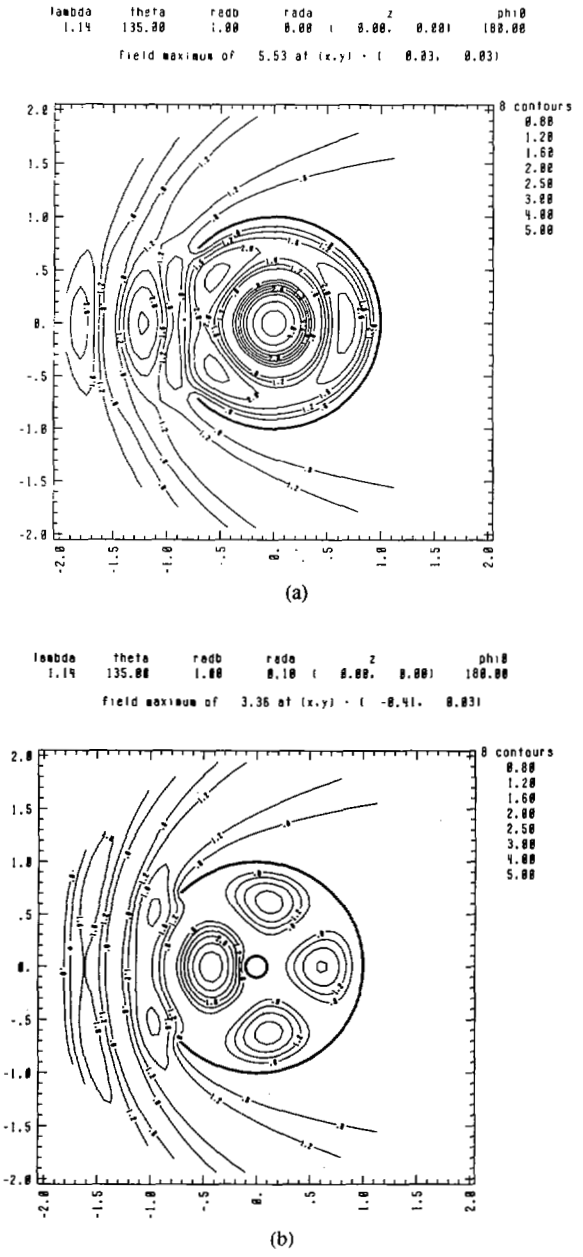

Fig. 8. The persistence of the cavity modes when the aperture is very large is shown by contour plots of the electric field generated by an E-pol plane wave with $\lambda = 1.138$ m incident from 180° upon a slit cylinder, $b = 1.0$ m and $2\Theta_{ap} = 90°$, when (a) it is empty, and (b) it encloses a wire with $a = 0.1$ m.

λ in Figs. 13(a) and 13(b). The substantial differences between the empty and loaded cylinder cases and between the two polarizations are interesting. The location of the hot spot in Fig. 12(a) suggests that the mechanism for hot-spot formation in the E-pol case is a focusing effect from the metallic surfaces. Similarly the wire in Fig. 13(a) acts like a reflector and causes the hot-spot to be located directly in front of it. On the other hand, a strong standing wave pattern is generated in the H-pol case as illustrated in Figs. 12(b) and 13(b). In particular, the field amplitudes exterior to the cylinder are not small. Moreover, the hottest spot appears in the aperture region of the cylinder rather than in its interior as in the E-pol case. This is due to the direct excitation by the plane wave of the edge singularity of the scattered electric field in the H-pol case. Furthermore, as shown in Fig. 13(b), the presence of the wire in the H-pol case causes a strong localization of the field near it. The wire radius has been increased to $a = 0.5\ \lambda$ in Fig. 14. In contrast to the E-pol case in Fig. 9(a), which is reproduced as Fig. 14(a), the H-pol case in Fig. 14(b) again shows the hot-spot forming in the aperture region. Moreover, the maximum hot spot amplitude in the H-pol case is approximately five times smaller than in the E-pol case. Fig.

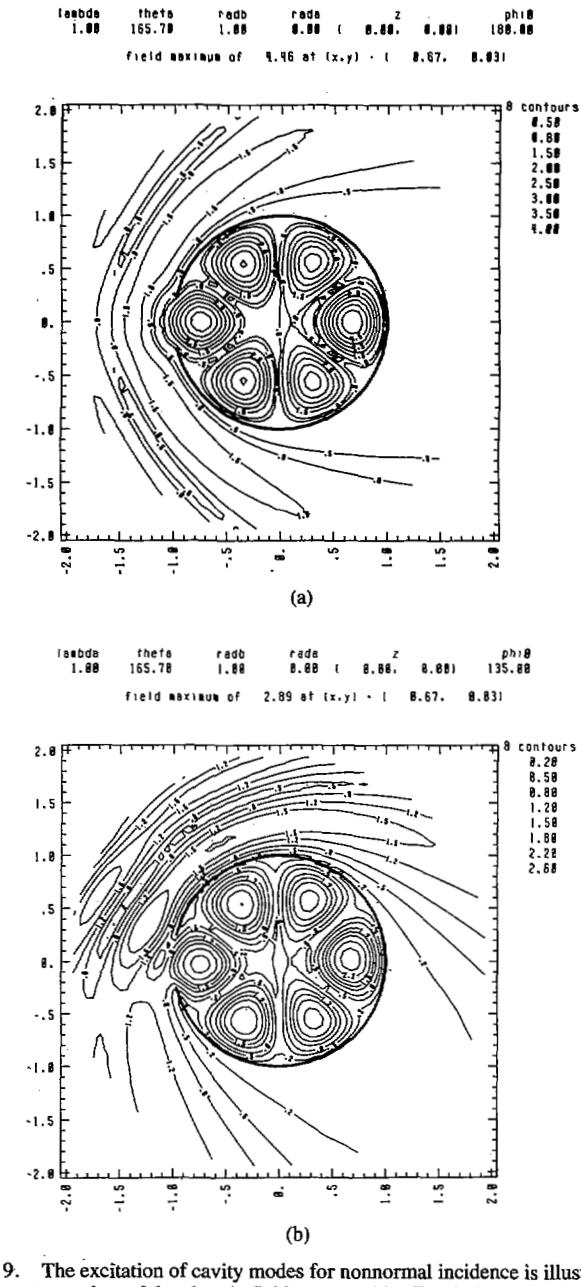

Fig. 9. The excitation of cavity modes for nonnormal incidence is illustrated by contour plots of the electric field generated by E-pol plane waves with $\lambda = 1.0$ m incident from (a) 180° and (b) 135° upon an empty slit cylinder, $b = 1.0$ m and $2\Theta_{ap} = 28.6°$.

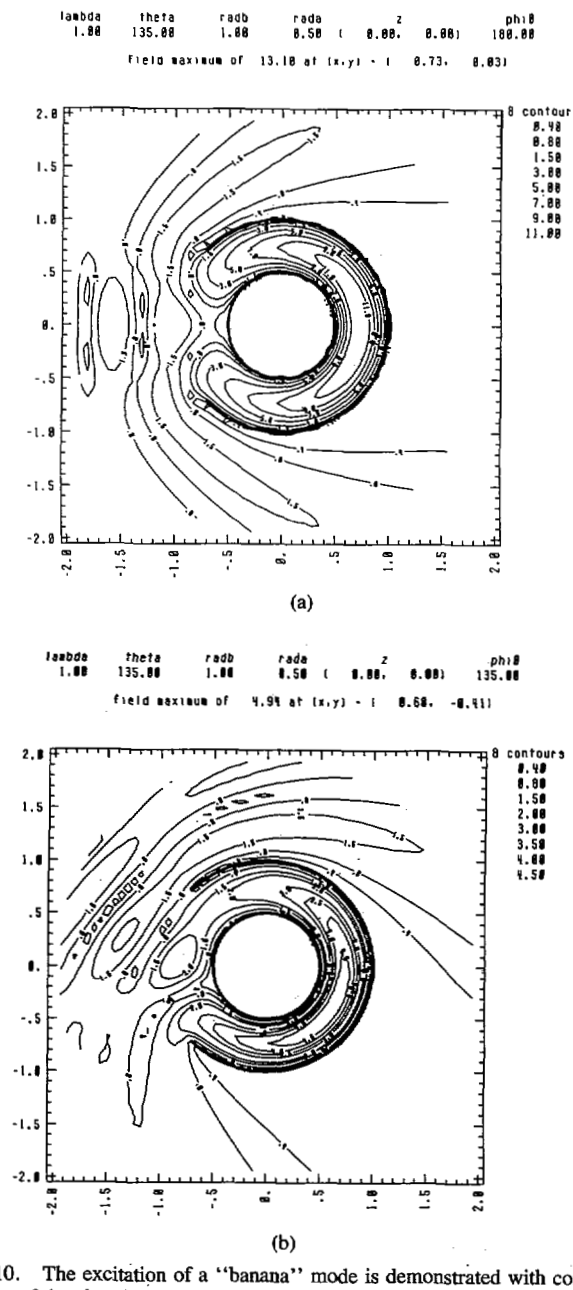

Fig. 10. The excitation of a "banana" mode is demonstrated with contour plots of the electric field generated by E-pol plane waves with $\lambda = 1.0$ m incident from (a) 180° and (b) 135° upon a slit cylinder, $b = 1.0$ m and $2\Theta_{ap} = 28.6°$, which encloses a wire with $a = 0.5$ m.

15 illustrates the closed waveguide mode formation in both the E-pol and the H-pol cases. The wave is incident from 180° and the angular extent of the aperture is 2° ($\Theta_{ap} = 1.0°$). Fig. 15(a) reproduces the TM_{02} results of Fig. 6(a); Fig. 15(b) illustrates the H-pol wave generating the TE_{01} waveguide mode. Again the hot-spot maximum is approximately five times lower in the H-pol case. On the other hand, the H-pol plane wave generates enhanced field amplitudes in the exterior of the slit cylinder as well as in its interior.

The E-pol slit cylinder solution also allows one to study the current I_z on the interior conductor as a function of frequency for all of the input parameters: angle of incidence, aperture size, wire size, and wire impedance. Figs. 16–18 represent one such parameter study. They show the *log* of the magnitude of the current (23) plotted against the *log* of the frequency for various configurations. The slit cylinder radius $b = 1.0$ m, the wire radius $a = 0.1$ m, and the E-pol plane wave is incident from 180°. In Fig. 16 the slit cylinder has $\Theta_{ap} = 1°$. In Fig. 16(a) the wire is taken to be perfectly conducting; in Fig. 16(b) it has a complex impedance $Z = (100.0, 100.0)$. These frequency scans are taken from 100 MHz to 1 GHz. The peaks in both figures directly correspond to the natural resonances of the closed coaxial guide. The effect of the complex impedance is seen to be 1) an upshift in the resonance locations, and 2) a

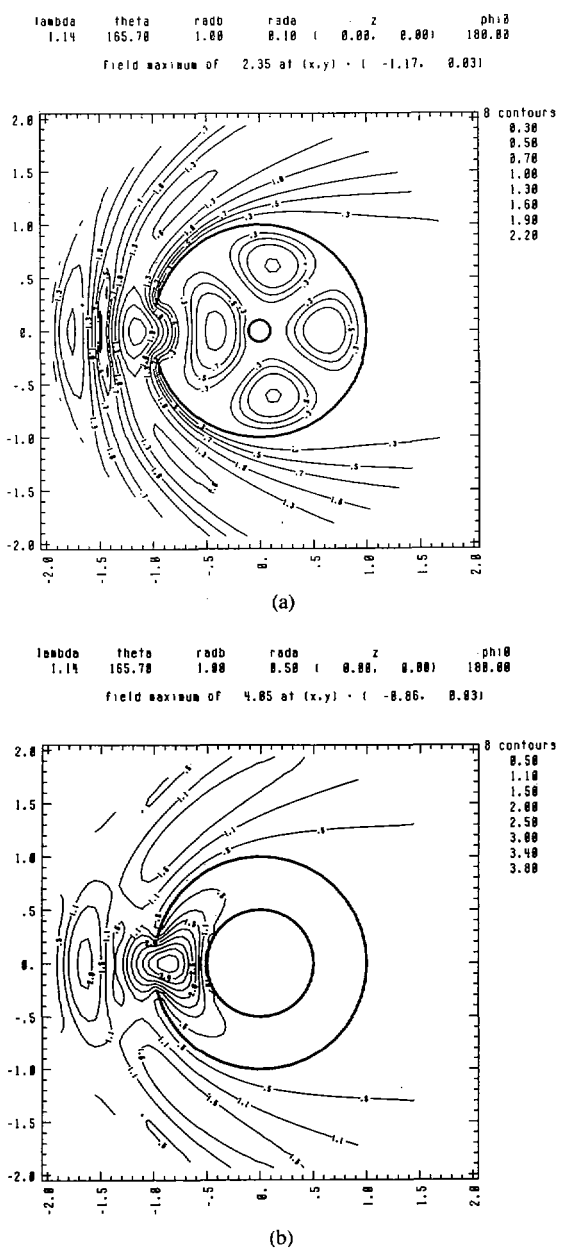

Fig. 11. Effects on the aperture coupling due to an increased interior wire radius are shown by comparing contour plots of the electric field generated by an E-pol plane wave with $\lambda = 1.138$ m incident from 180° upon a slit cylinder, $b = 1.0$ m and $2\Theta_{ap} = 28.6°$, which encloses wires with (a) $a = 0.1$ m and (b) $a = 0.5$ m.

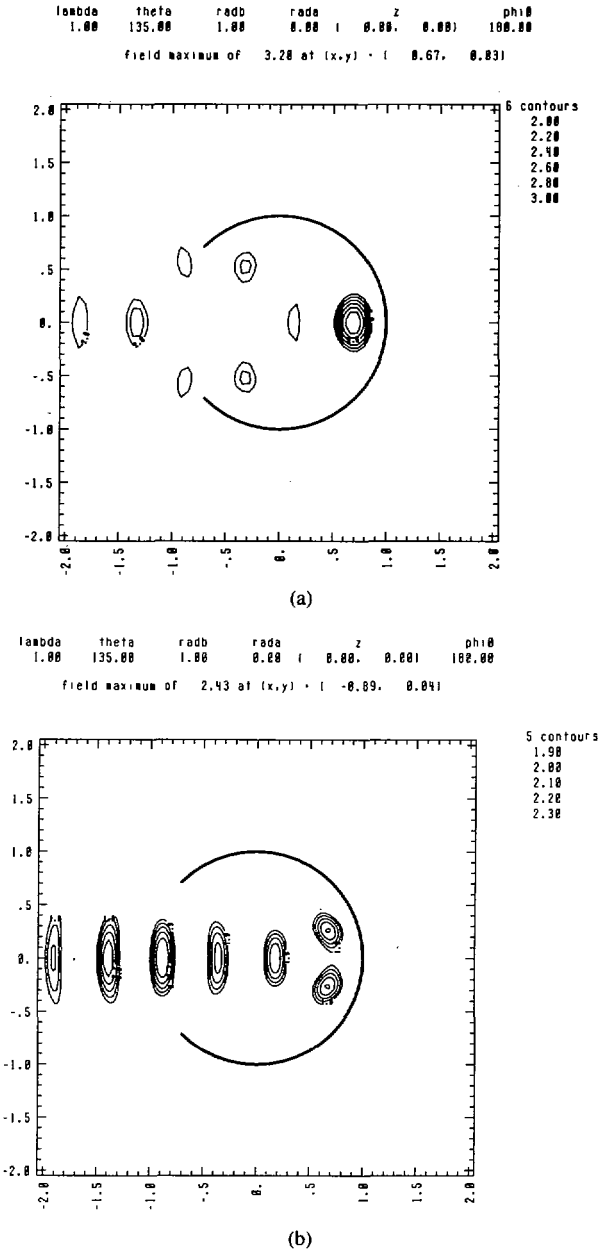

Fig. 12. Polarization effects on the aperture coupling are illustrated with contours plots of the electric field generated by (a) E- and (b) H-pol plane waves incident from 180° upon an empty slit cylinder, $b = 1.0\ \lambda$ and $2\Theta_{ap} = 90°$.

broadening of the resonance peaks. The small irregularities in the data are less pronounced resonances due to the proliferation of modes as the frequency is increased. Those in the frequency range: 100–400 MHz, in Fig. 16(a) are shown on an expanded scale in Fig. 17(a) and have been enhanced by a finer sampling in frequency. These resonance features are very narrow and are indicative of the extremely high Q nature of the cavity. Moreover, they are further enhanced by increasing the aperture size as shown by Fig. 17(b) where the angular extent of the aperture is now 10° ($\Theta_{ap} = 5°$). The "antiresonance" form of these peaks was not anticipated. It is actually the predominant form of the resonant peaks. A careful analysis of the natural frequencies of the coaxial guide indicates that the "standard" form of resonance peak occurs only at the TM_{0n} mode frequencies. For example, the resonant peaks at 8.199 and 8.515 correspond to the TM_{01} and TM_{02} modes while the antiresonances at 8.274, 8.389, 8.483, 8.544, and 8.556 correspond to the TM_{11}, TM_{21}, TM_{31}, TM_{12}, and TM_{41} modes. The importance of these antiresonance features increases as the aperture size is increased as shown in Fig. 18. Fig. 17(b) is reproduced as Fig. 18(a); the angular extent of the aperture in Fig. 18(b) is 30° ($\Theta_{ap} = 15°$). The background level of the current has risen because the incident field

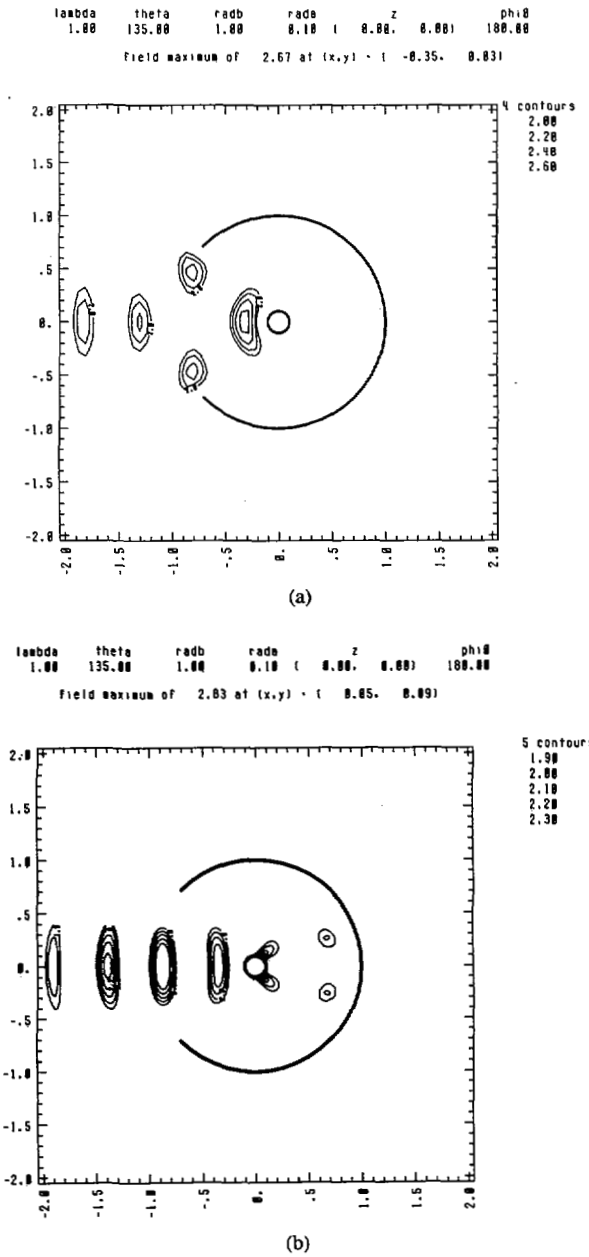

Fig. 13. Polarization effects on the aperture coupling are illustrated with contour plots of the electric field generated by (a) E- and (b) H-pol plane waves incident from 180° upon a slit cylinder, $b = 1.0\ \lambda$ and $2\Theta_{ap} = 90°$, which encloses a wire with $a = 0.1\ \lambda$.

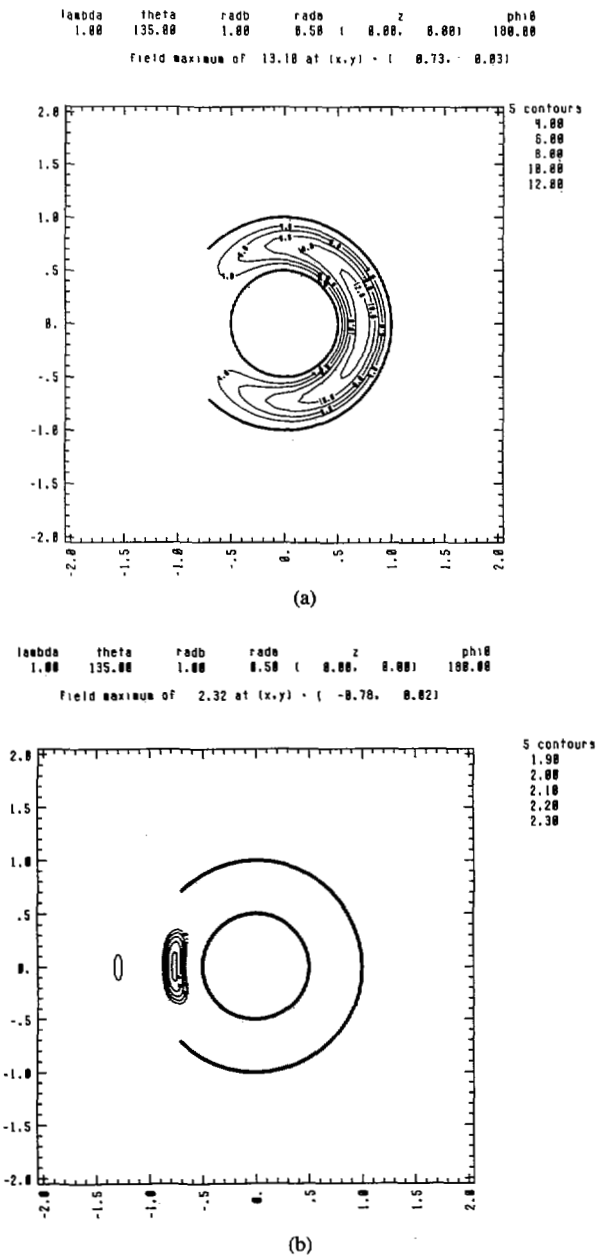

Fig. 14. Polarization effects on the aperture coupling are illustrated with contour plots of the electric field generated by (a) E- and (b) H-pol plane waves incident from 180° upon a slit cylinder, $b = 1.0\ \lambda$ and $2\Theta_{ap} = 90°$, which encloses a wire with $a = 0.5\ \lambda$.

penetrates more readily into the interior of the cavity. The resonant peaks have become substantially detuned while the antiresonance structures become broader with more pronounced minimums.

Sample cross-section results are presented in Figs. 19–22. In Figs. 19 and 20 kb scans of the radar (RCS) and forward (FCS) cross sections are given for a plane wave incident from 180.0° on a slit cylinder with a radius of $b = 1.0$ m and a 10° aperture ($\Theta_{ap} = 5.0°$). The RCS is defined by the angles ($\phi_0 = 180.0°$, $\phi = 180.0°$); the FCS by ($\phi_0 = 180.0°$, $\phi = 0.0°$). The cylinder is empty in Fig. 19; it is loaded with a perfectly conducting wire of radius $a = 0.3$ m in Fig. 20. Figs. 19(a) and 20(a) are the E-pol results, Figs. 19(b) and 20(b) the H-pol results. The slit cylinder cases are represented by solid lines; the asterisks in each figure represent the corresponding closed cylinder cross sections.

It is seen in Figs. 19 and 20 that except for the presence of resonance features, the E-pol RCS and the H-pol FCS closely follow the corresponding closed cylinder results. Note that although they are barely discernible in the E-pol RCS, resonance features are present at locations corresponding to those in the FCS. In contrast, the E-pol FCS and the H-pol RCS deviate from the corresponding closed cylinder results. Except for the low frequency peaks in the H-pol cases, the

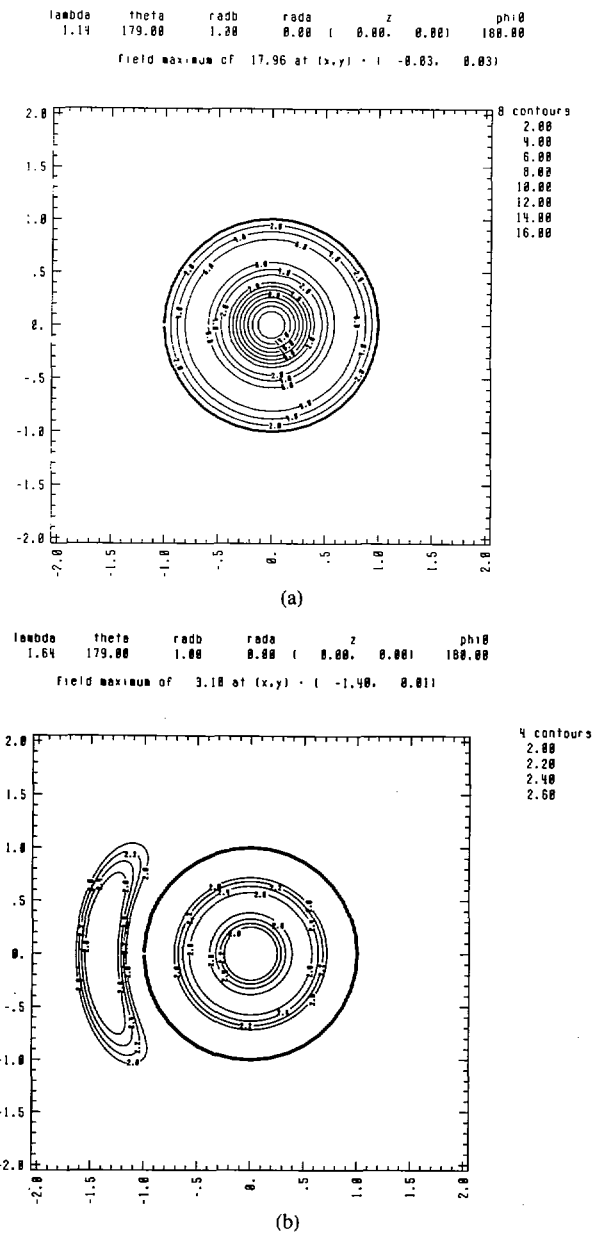

Fig. 15. Coupling to the natural modes of the open cavity formed by an empty slit cylinder, $b = 1.0$ m and $2\Theta_{ap} = 2°$, is obtained with E- and H-pol plane waves at particular wavelengths. (a) The TM_{02} circular waveguide mode is excited by an E-pol plane wave incident from 180° with $\lambda = 1.138$ m. (b) The TE_{01} circular waveguide mode is excited by an H-pol plane wave incident from 180° with $\lambda = 1.640$ m.

locations of the resonance features in the cross sections depend intimately on the location of the resonances of the interior cavity. In particular, for the E-pol case in Fig. 19(a) the peaks of the FCS occur at kb values of 2.39, 3.82, 5.12, 5.51, and 6.37 which correspond to the TM_{01}, TM_{11}, TM_{21}, TM_{12}, and TM_{31} waveguide modes. These mode assignments were made by plotting the field patterns at those kb values and comparing them with the ones given in [11, p. 207]. These slit cylinder resonances occur at kb values which are slightly lower than those of the closed cylinder: 2.41, 3.83, 5.14, 5.52, and 6.38. For the corresponding H-pol case the peaks of the RCS occur at kb values of 0.37, 1.96, 3.15, 3.85, 4.29, 5.33, and 5.44 and, excepting the low-frequency peak at $kb = 0.37$, correspond to the TE_{11}, TE_{21}, TE_{01}, TE_{31}, TE_{12}, and TE_{41} waveguide modes. The TE_{n1} mode locations are slightly higher than those of the closed cylinder: 1.84, 3.05, 3.83, 4.20, and 5.32; while the TE_{12} mode location has remained the same as the closed cylinder's: 5.33. Thus the sequence of appearance of the modal patterns has also changed in the open cylinder case.

The H-pol low frequency resonance has been explained in terms of an equivalent LC circuit by Warne [7]. The aperture causes a break in the (transverse) current on the outer, open cylinder which results in an equivalent capacitance and inductance. As seen in the H-pol RCS and FCS curves, the slit cylinder strongly radiates at this low frequency resonance. The resonance peaks in the cross sections that are connected to the cavity resonances are indicative of a reradiation phenomena that is associated with the cavity-backed nature of the aperture. The currents induced on the slit cylinder and consequently the scattered fields experience a π-phase shift as kb passes through one of these cavity-backed aperture (CBA) resonances. Thus a scattered field is created that at different look angles either constructively or destructively interferes with the incident field. This results, for instance, in the distinctive antiresonance features present in the E-pol FCS and the H-pol RCS. Consider one of these H-pol RCS antiresonances and the associated FCS resonance feature in Fig. 19(b). The enhancement of the field in the backscattered direction is followed by a corresponding decrease in the forward scattered signal as one approaches a CBA resonance location from the low kb side. As kb passes through such a CBA resonance value, there is a dramatic decrease in the RCS level followed by an increase in unison of both the FCS and RCS levels as kb increases further. The reason that the E-pol RCS response is so low in comparison to the H-pol response is attributed to the current patterns on the slit cylinder. As kb approaches any of the TE_{n1} H-pol CBA resonances, the current peaks nearest the aperture edges diminish in size while those away from the aperture increase. The FCS shows a null while the RCS has a peak. In contrast, the current near the edge of the aperture is also enhanced at the TE_{12} CBA resonance and one sees mirror-imaged antiresonances in the RCS and FCS responses. Analogously the E-pol slit cylinder current always has an infinity at the aperture edge. When an E-pol CBA resonance is encountered, there are small RCS but large FCS responses. Thus we find that the current behavior near the aperture edge governs the FCS response; its behavior away from the aperture is responsible for the RCS response.

The resonance locations in a closed coax waveguide are shifted from those in an empty guide. For instance, one observes the sequence in which resonances appear to be altered and a disappearance of some resonances in a fixed kb interval. One would then expect a similar movement in the resonance features in the cross sections. These effects are demonstrated in Fig. 20. For the E-pol case the peaks of the FCS are now at kb values of 4.41, 4.69, 5.46, and 6.48. These

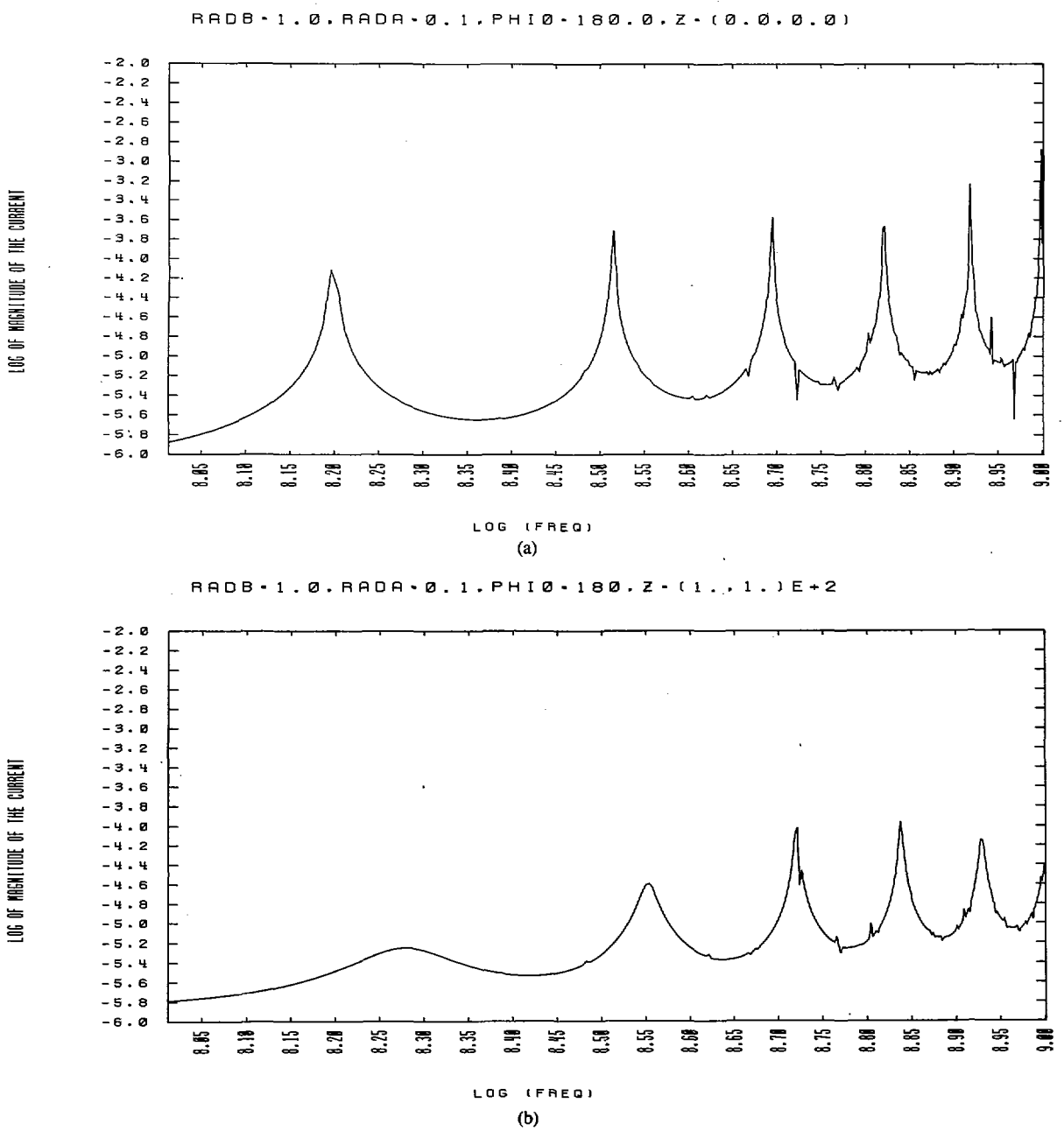

Fig. 16. Cavity-backed aperture resonance effects are illustrated with frequency scans of the current I_z induced on a wire with a = 0.1 m in the interior of a slit cylinder, b = 1.0 m and $2\Theta_{ap} = 2°$, by an E-pol plane wave incident from 180° when (a) the wire is perfectly conducting, and (b) the wire has a complex impedance Z = (100.0,100.0).

CBA resonances correspond to the TM_{01}, TM_{11}, TM_{21}, and TM_{31} waveguide modes of the coax configuration. The location of the resonances are all at higher kb values. The resonance feature corresponding to the TM_{12} mode present in Fig. 19(a) is absent here because it has migrated to a kb value greater than 7.0. For the corresponding H-pol case the resonance peaks of the RCS now occur at kb values of 0.39, 1.71, 3.06, 4.27, 5.17, and 5.41. The CBA resonances correspond to the TE_{11}, TE_{21}, TE_{31}, TE_{01} and TE_{41} coax modes. The location of the TE_{11} CBA resonance is at a lower kb value while the other ones are all at higher kb values. The resonance feature corresponding to the TE_{12} mode present in Fig. 19(b) is absent here because it has migrated to a kb value greater than 6.0. Note that the mode number assignments were made by comparing the field patterns at the CBA resonances to those of the closed waveguide given in [12, pp. 77–79].

The presence of these resonance features in the monostatic cross sections even for normal incidence away from the aperture is illustrated with Fig. 21. The H-pol RCS and FCS curves are given for the same geometry as in Fig. 19 except that the field is now incident from 0.0°. The peaks of the RCS resonance features are much smaller and the general response

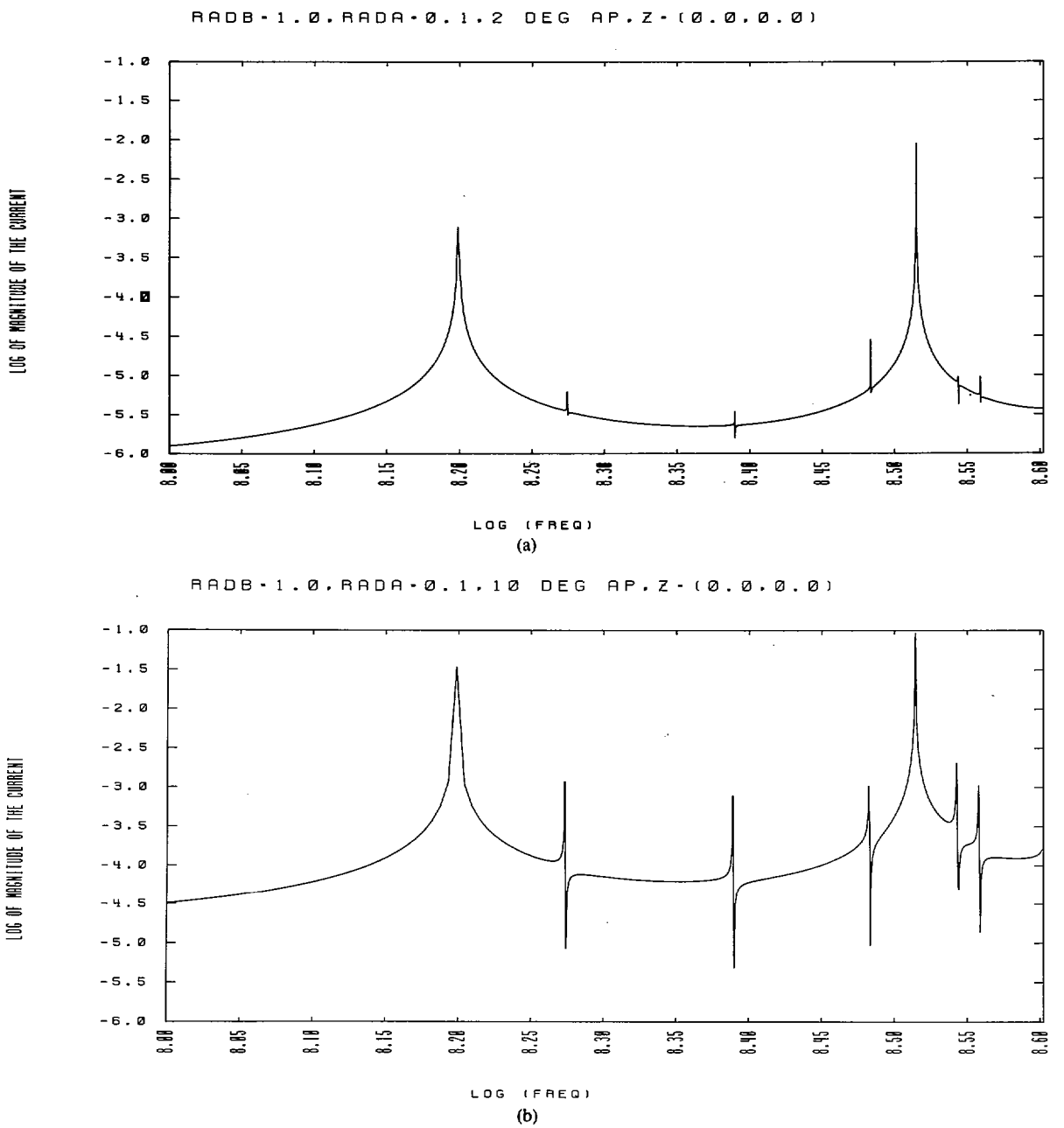

Fig. 17. Frequency scans of the current induced on a perfectly conducting wire with $a = 0.1$ m in the interior of a slit cylinder, $b = 1.0$ m, by an E-pol plane wave incident from 180°, when $2\Theta_{ap}$ is varied from (a) 2° to (b) 10° illustrate the effects an increased aperture size has on the I_z CBA resonance features.

deviates less from the closed cylinder RCS. In contrast, the FCS when the plane wave sees the aperture (Fig. 19(b)) and when it sees the metal (Fig. 21(b)) are identical! Although it is not discernable in the Fig. 21(a), there is a CBA resonance feature at $kb = 5.33$ in the RCS.

Fig. 22 illustrates the effect of impedance on the H-pol RCS and FCS responses. The configuration is the same as in Fig. 20(b) except that the interior cylinder has the complex impedance $Z = (100.0,100.0)$. One finds that the low frequency response is diminished and the TE_{01} CBA resonance has been completely damped out. On the other hand, there is an enhancement of the responses due to the TE_{11}, TE_{21}, and TE_{41} CBA resonances despite the load being lossy. In comparison the E-pol CBA resonance features are completely damped out by the lossy load and the cross sections are nearly identical to the corresponding closed cylinder case. These results are again closely related to the modal structure at the CBA resonances. When the wire is perfectly conducting, all of the E-pol and the H-pol TE_{0n} resonance patterns are dominated by maximums near it. These maximums and hence, the interior fields, are radically damped when the wire is lossy. This results in the reduced cross-section responses. In contrast

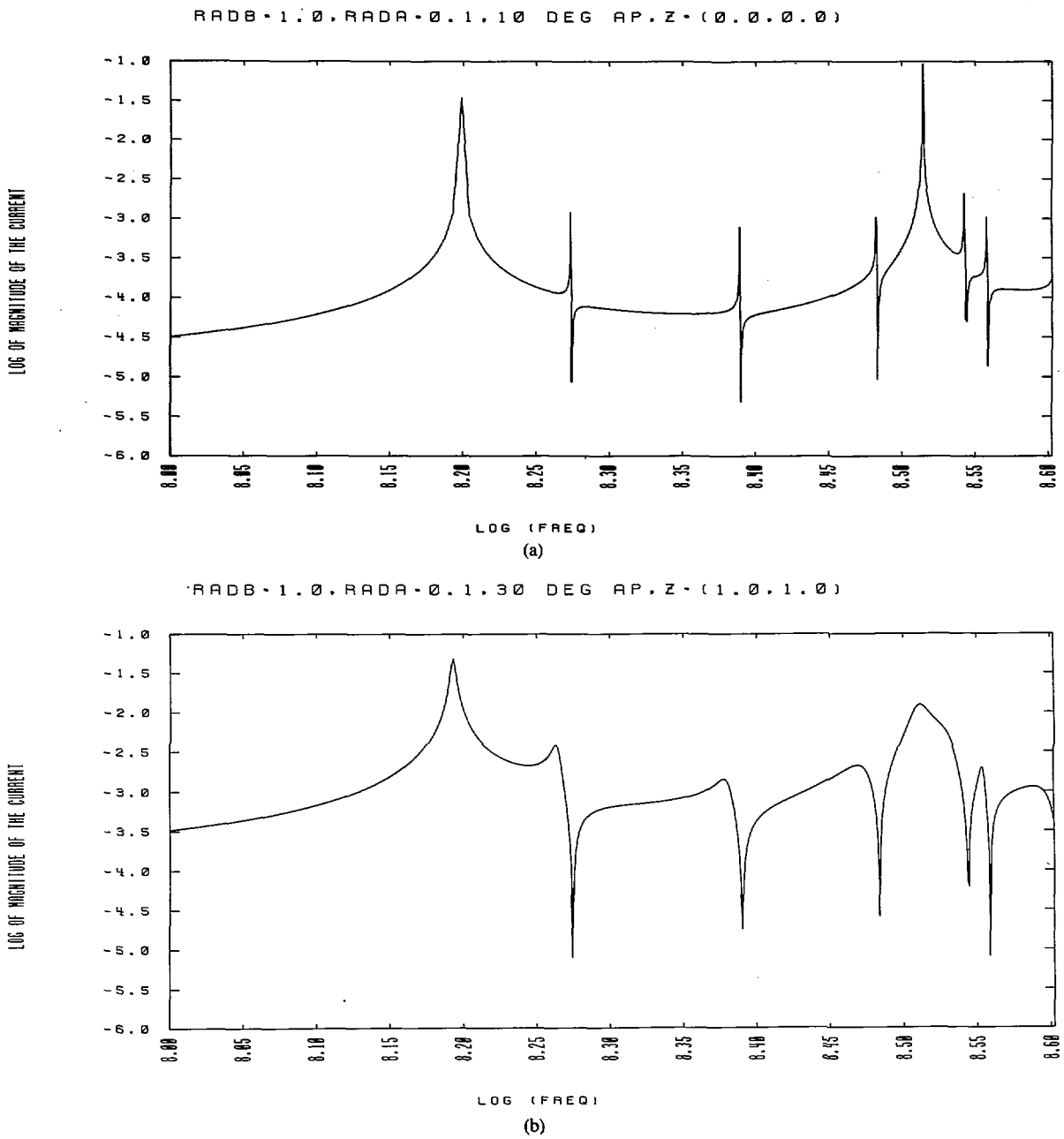

Fig. 18. Frequency scans of the current induced on a perfectly conducting wire with $a = 0.1$ m in the interior of a slit cylinder, $b = 1.0$ m, by an E-pol plane wave incident from 180°, when $2\Theta_{ap}$ is varied from (a) 10° to (b) 30° illustrate the effects an even larger aperture size has on the I_z CBA resonance features.

the wire rests in a depression of the other H-pol CBA resonance patterns so that when the wire is lossy, it does not significantly alter the structure of the modal patterns. The lossy load does tend to pull the H-pol current peaks away from the aperture and enhances the peak directly opposite the aperture near $\phi = 0.0°$. This explains the significant increases in the RCS curves shown in Fig. 22(a). In addition for the TE_{41} case it actually increases the interior field maximums by enhancing the definition of the basic modal pattern. The result is an overall increase in the current peaks which explains the corresponding enhancement of the associated FCS CBA resonance feature in Fig. 22(b).

These resonance features are also found in the bistatic cross sections at the same relative positions for at all look angles. This is true even for not normal incidence. As one might expect, the shapes and sizes of the individual resonance peaks vary with the angle of incidence and the relative bistatic look angles.

V. Conclusion

Parameter studies of the generalized dual series solutions to the concentrically loaded E-pol and H-pol slit cylinder canonical problems are enhancing our understanding of the aperture coupling process and are continuing. The examples presented above illustrate how we have used the current and

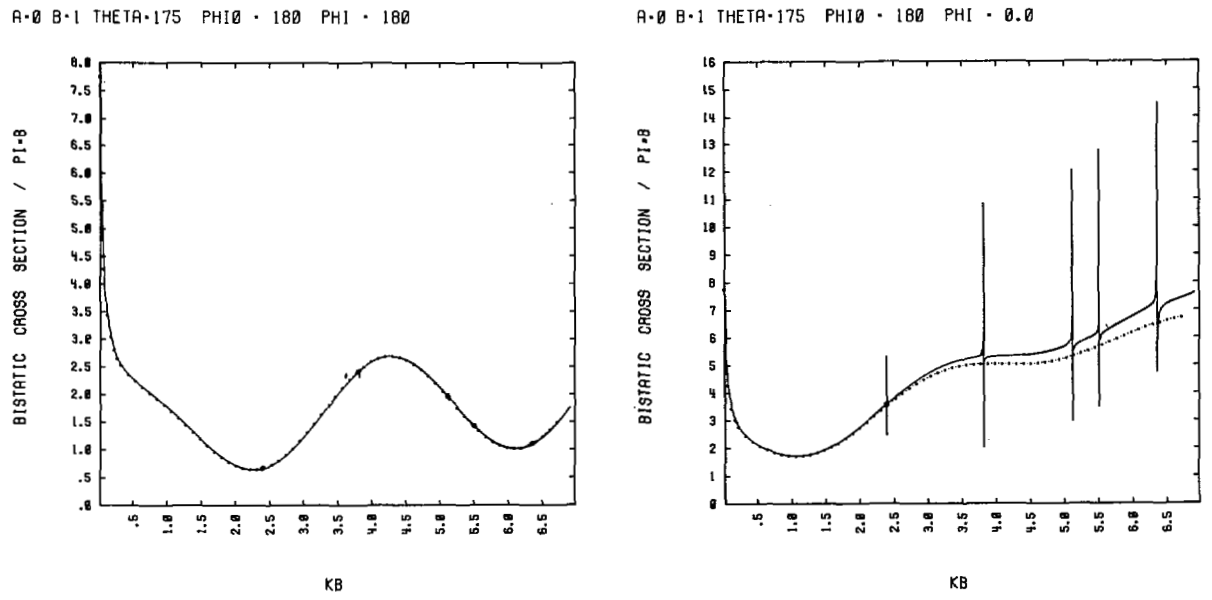

Fig. 19. The presence of CBA resonance features in the exterior scattering data is demonstrated with scans (solid lines) in kb of the back (radar) and forward scattered cross sections resulting from (a) E-pol and (b) H-pol plane waves incident from 180° on an empty slit cylinder, $b = 1.0$ m and $2\Theta_{ap} = 10°$. The corresponding closed cylinder cross sections are represented by the asteriks.

field patterns to estimate the amount of field penetration into the interior cavity for various polarizations, loads, angles of incidence, and aperture size. With these results we are trying to establish "engineering" models of the aperture coupling that can be applied to more general aperture and cavity shapes.

The presence of the resonance features in the E-pol interior wire currents and in the E- and H-pol cross sections are extremely interesting. What role, if any, the current resonances may play in EMP damage mechanisms is being examined. The cross-section resonances indicate that *for cavity-backed apertures there is interior information contained in the exterior scattering data.* The dependence of the location of these peaks on the interior structure and their presence at all look angles may have very important ramifications for object identification applications. These resonance peaks are also being analyzed in the cross sections resulting from plane wave scattering from a slit cylinder with an offset interior impedance surface [13], from an empty open spherical shell with a circular aperture [14], and from an open spherical shell with a circular aperture enclosing either a concentric metallic or dielectric sphere [15]. The results of these investigations will be the topics of several future papers.

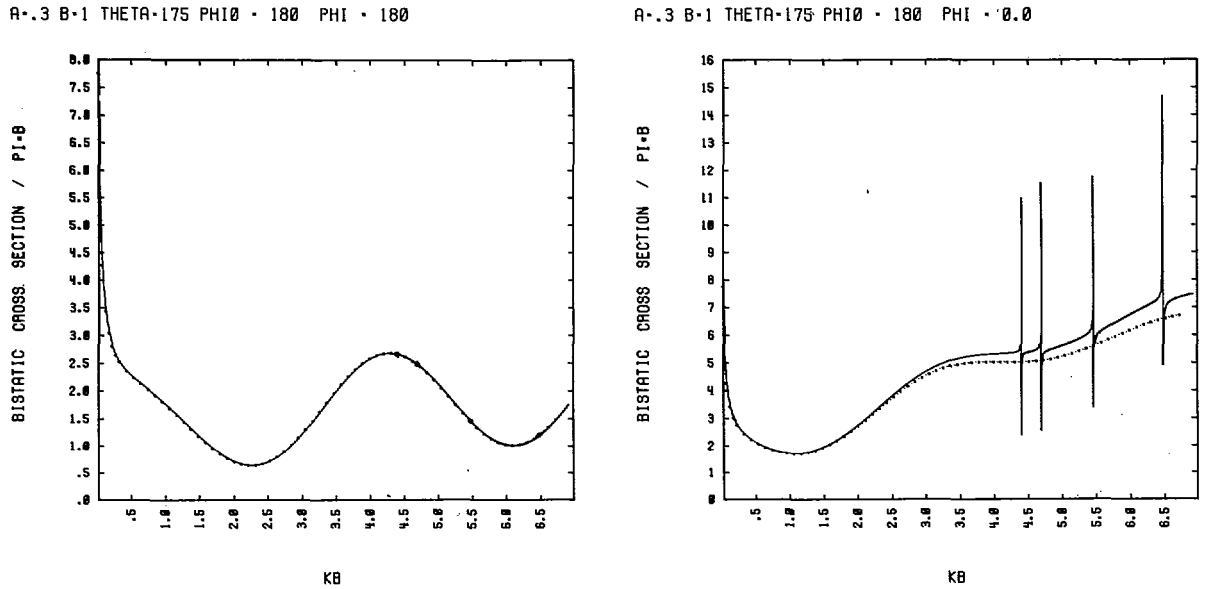

(a)

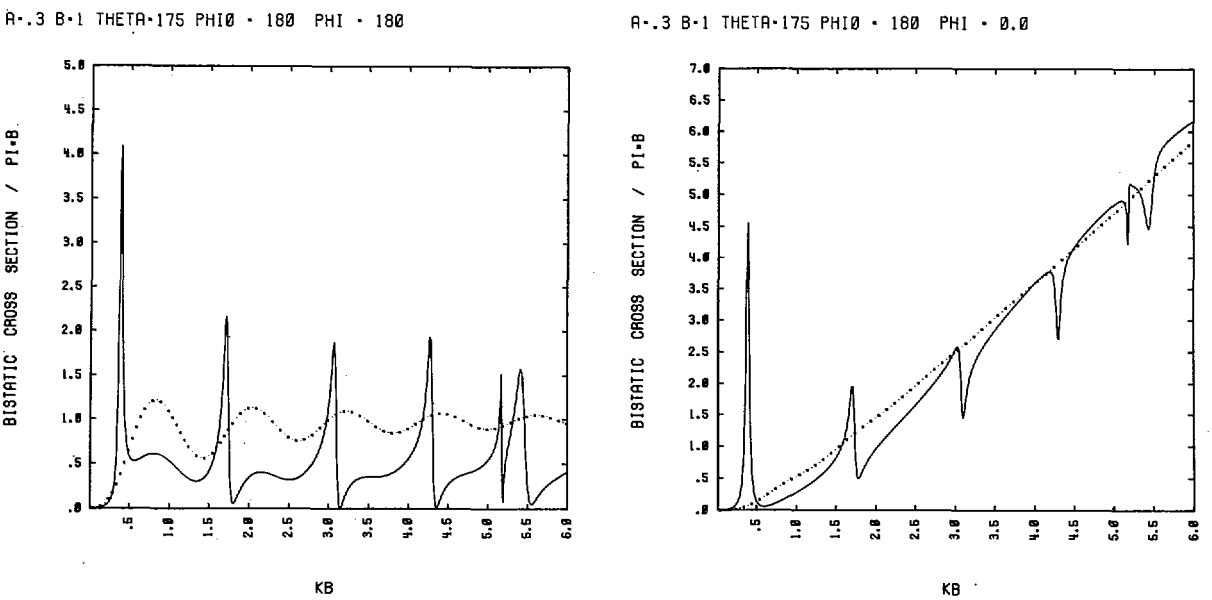

(b)

Fig. 20. The dependence of the CBA resonance features in the exterior scattering data on the interior of the open cavity is demonstrated with scans (solid lines) in kb of the back (radar) and forward scattered cross sections resulting from (a) E-pol and (b) H-pol plane waves incident from 180° on a slit cylinder, $b = 1.0$ m and $2\Theta_{ap} = 10°$, which encloses a perfectly conducting wire of radius 0.3 m. The corresponding closed cylinder cross sections are represented by the asteriks.

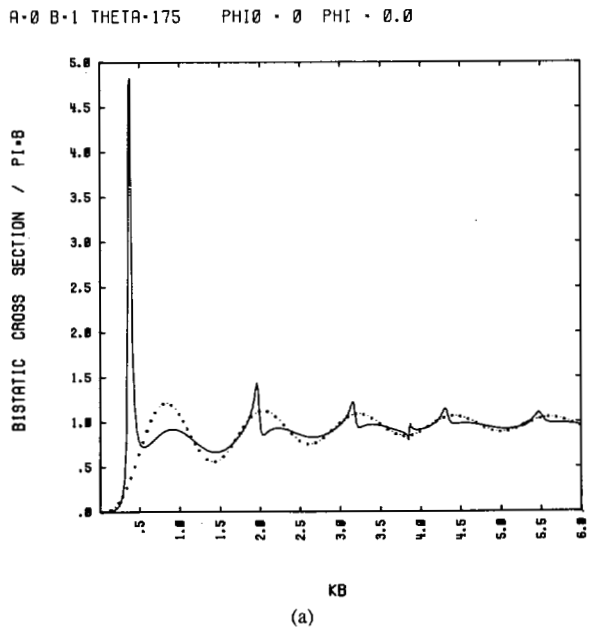

(a)

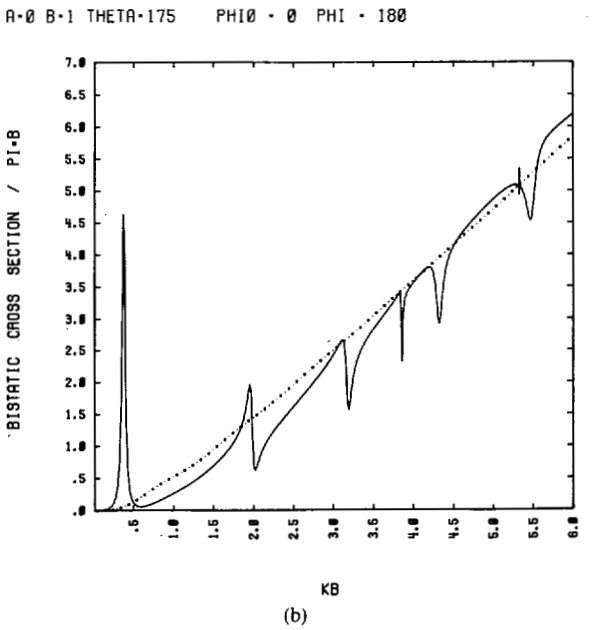

(b)

Fig. 21. The presence of the CBA resonance features in the exterior scattering data even for nonnormal incidence is illustrated with scans (solid lines) in kb of the back (radar) and forward scattered cross sections resulting from an H-pol plane wave incident from 0° on an empty slit cylinder, $b = 1.0$ m and $2\Theta_{ap} = 10°$. The corresponding closed cylinder cross sections are represented by the asteriks.

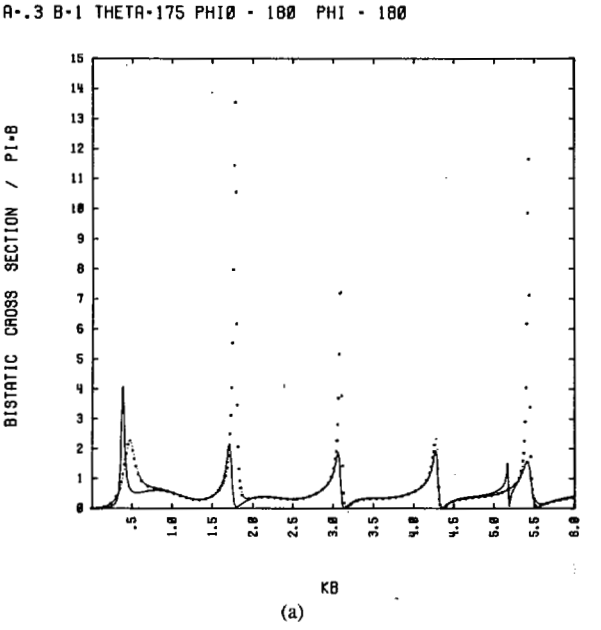

(a)

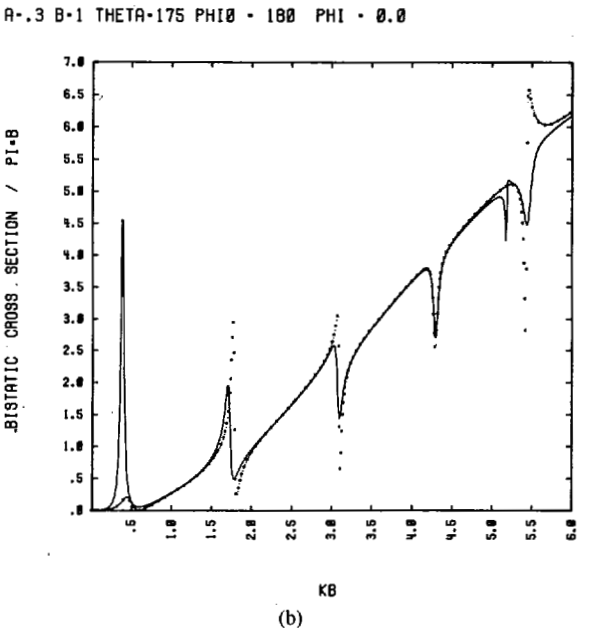

(b)

Fig. 22. The effects of a lossy interior wire has on the CBA resonance features in the exterior scattering data is illustrated with scans in kb of the back (radar) and forward scattered cross sections resulting from an H-polarized plane wave incident from 180° on a slit cylinder, $b = 1.0$ m and $2\Theta_{ap} = 10°$, which encloses (a) a perfectly conducting wire (solid lines) and (b) an impedance surface with $Z = (100.0,100.0)$ (asteriks) of radius 0.3 m.

Appendix I
Limiting Behavior of Dual Series Coefficients

In the limits of either small argument ($z \ll 1$) or large index ($n \to \infty$) the series expansions [16] of the Bessel and the Hankel functions and their derivatives yield

$$J_n \sim \frac{1}{n!}\left(\frac{z}{2}\right)^n \left[1 - \frac{1}{(n+1)}\left(\frac{z}{2}\right)^2\right]$$

$$H_n \sim \frac{(n-1)!}{-j\pi}\left(\frac{z}{2}\right)^{-n} \left[1 + \frac{1}{(n-1)}\left(\frac{z}{2}\right)^2\right]$$

$$J_n' \sim \frac{1}{2(n-1)!}\left(\frac{z}{2}\right)^{n-1} \left[1 - \frac{n-2}{n(n+1)}\left(\frac{z}{2}\right)^2\right]$$

$$H_n' \sim \frac{n!}{2j\pi}\left(\frac{z}{2}\right)^{-(n+1)} \left[1 + \frac{n-2}{n(n-1)}\left(\frac{z}{2}\right)^2\right].$$

Therefore, in these limits one has

$$J_{|n|}(z)H_{|n|}(z) \sim \frac{1}{(-j\pi|n|)}\left[1 + \frac{2}{|n|^2 - 1}\left(\frac{z}{2}\right)^2\right]$$

$$\Omega_{|n|}(z)\sim\frac{-j\pi}{|n|!(|n|-1)!}\left(\frac{z}{2}\right)^{2|n|}\begin{cases}+1, & \text{if } Z\neq 0\\ -1, & \text{if } Z=0\end{cases}$$

$$\frac{J_{|n|}(y)}{J_{|n|}(z)}\sim\left(\frac{y}{z}\right)^{|n|}\qquad\frac{J'_{|n|}(y)}{J_{|n|}(z)}\sim\frac{|n|}{z}\left(\frac{y}{z}\right)^{|n|-1}$$

$$\frac{H_{|n|}(y)}{H_{|n|}(z)}\sim\left(\frac{z}{y}\right)^{|n|}\qquad\frac{H'_{|n|}(y)}{H_{|n|}(z)}\sim-\frac{|n|}{y}\left(\frac{z}{y}\right)^{|n|}$$

$$\frac{H_{|n|}(y)}{J_{|n|}(z)}\sim\frac{j}{\pi}\,|n|!(|n|-1)!\left(\frac{4}{yz}\right)^{|n|}$$

$$\frac{H'_{|n|}(y)}{J'_{|n|}(z)}\sim-\frac{j}{\pi}\,|n|!(|n|-1)!\left(\frac{z}{y}\right)\left(\frac{4}{yz}\right)^{|n|}$$

so that the expressions

$$\alpha_{|m|}(kb)H_{|m|}(kb)$$

$$=J_{|m|}(kb)H_{|m|}(kb)\left\{1-\frac{J_{|m|}(ka)H_{|m|}(kb)}{J_{|m|}(kb)H_{|m|}(ka)}\cdot\left[\frac{1-(Z/jZ_0)(J'_{|m|}(ka)/J_{|m|}(ka))}{1-(Z/jZ_0)(H'_{|m|}(ka)/H_{|m|}(ka))}\right]\right\}$$

$$\sim\frac{1}{(-j\pi|m|)}\left[1+\frac{2}{|m|^2-1}\left(\frac{kb}{2}\right)^2\right]\left[1\mp\left(\frac{a}{b}\right)^{2|m|}\right]\cdot\begin{cases}\text{upper sign if } Z=0\\ \text{lower sign if } Z\neq 0\end{cases}$$

$$\frac{H'_{|m|}(kr)}{H_{|m|}(kb)}\sim-\frac{|m|}{kr}\left(\frac{b}{r}\right)^{|m|}$$

$$\frac{\alpha_{|m|}(kr)}{\alpha_{|m|}(kb)}=\frac{J_{|m|}(kr)}{J_{|m|}(kb)}\cdot\left\{\frac{1+\Omega_{|m|}(ka)[H_{|m|}(kr)/J_{|m|}(kr)]}{1+\Omega_{|m|}(ka)[H_{|m|}(kb)/J_{|m|}(kb)]}\right\}\sim\left(\frac{r}{b}\right)^{|m|}$$

$$\frac{\alpha'_{|m|}(kr)}{\alpha_{|m|}(kb)}=\frac{J'_{|m|}(kr)}{J_{|m|}(kb)}\cdot\left\{\frac{1+\Omega_{|m|}(ka)[H'_{|m|}(kr)/J'_{|m|}(kr)]}{1+\Omega_{|m|}(ka)[H_{|m|}(kb)/J_{|m|}(kb)]}\right\}\sim\frac{|m|}{kb}\left(\frac{r}{b}\right)^{|m|-1}.$$

Consequently one has from (8b) and (10) that for $kb\ll 1$

$$\chi_m=\frac{\tau_m}{|m|}-1\sim\frac{\pm(a/b)^{2|m|}}{1\mp(a/b)^{2|m|}}\begin{cases}\text{upper sign if } Z=0\\ \text{lower sign if } Z\neq 0\end{cases}$$

$$\tau_m=|m|(1+\chi_m)\sim\frac{|m|}{1\mp(a/b)^{2|m|}}\begin{cases}\text{upper sign if } Z=0\\ \text{lower sign if } Z\neq 0\end{cases}$$

and for $m\to\infty$

$$\chi_m\sim\left[1+\frac{2}{|m|^2-1}\left(\frac{kb}{2}\right)^2\right]^{-1}-1\sim-\frac{1}{2}\left(\frac{kb}{|m|}\right)^2$$

$$\tau_m\sim|m|.$$

Appendix II
Coefficient Definitions

The inversion coefficients V_m^n for $m\neq n$ are given by the expression:

$$V_m^n=\frac{m+1}{2(m-n)}\left[P_m(u)P_{n+1}(u)-P_{m+1}(u)P_n(u)\right].$$

The special case when $m=n$ is given by

$$V_n^n=\frac{n+1}{2}\left[U_n(u)P_{n+1}(u)-U_{n+1}(u)P_n(u)\right]$$

where

$$U_0(u)=0$$

$$U_1(u)=u-1$$

$$U_{n+1}(u)=\frac{uP_n(u)-P_{n-1}(u)}{(n+1)^2}+\frac{2n+1}{n+1}\,uU_n(u)-\frac{n}{n+1}\,U_{n-1}(u)$$

and

$$P_{-n}(u)=P_{n-1}(u)$$

$$U_{-n}(u)=U_{n-1}(u).$$

The remaining coefficient terms are defined as

$$W^n=-\frac{1}{2}\,\mu_{n+1}(u)\ln\left(\frac{1+u}{2}\right)+\frac{1}{2n}\left[P_n(u)-P_{n-1}(u)\right]$$

$$S=\frac{1}{2}\sum_{m\neq 0}(-)^m\frac{P_m(u)}{m}=-\frac{1}{2}\ln\left(\frac{1+u}{2}\right)$$

where

$$u=\cos(\Theta)$$

and

$$\mu_0(u)=1\quad\mu_1(u)=-P_1(u)=-u$$

$$\mu_n(u)=P_n(u)-2uP_{n-1}(u)+P_{n-2}(u),\qquad\text{for } (n\geq 2).$$

Appendix III
Current Sum Formula

The current sum formula (22′) follows from the summation formulas [17]

$$\sum_{m=0}^{\infty}P_m(\cos\Theta)\sin m\phi$$

$$=\begin{cases}-\sin\dfrac{\phi}{2}\left[2(\cos\phi-\cos\Theta)\right]^{-1/2}, & (\phi<\Theta)\\ -\cos\dfrac{\phi}{2}\left[2(\cos\Theta-\cos\phi)\right]^{-1/2}, & (\phi>\Theta)\end{cases}$$

$$\sum_{m=0}^{\infty} P_m(\cos\Theta)\cos m\phi = \begin{cases} +\cos\dfrac{\phi}{2}\,[2(\cos\phi-\cos\Theta)]^{-1/2}, & (\phi<\Theta) \\ -\sin\dfrac{\phi}{2}\,[2(\cos\Theta-\cos\phi)]^{-1/2}, & (\phi>\Theta) \end{cases}$$

which lead to the following relations for $\phi > \Theta$:

$$S_+(\phi) \equiv \sum_{m=0}^{\infty} P_m e^{jm\phi} = -\frac{je^{-j\phi/2}}{[2(\cos\Theta-\cos\phi)]^{1/2}}$$

$$S_-(\phi) \equiv \sum_{m=0}^{\infty} P_m e^{-jm\phi} = +\frac{je^{+j\phi/2}}{[2(\cos\Theta-\cos\phi)]^{1/2}}.$$

In particular, with (22) one has

$$\begin{aligned} \tilde{J}_s(\phi) &= \kappa_1\left(\sum_{m=1}^{\infty} P_m e^{jm\phi} - \sum_{m=1}^{\infty} P_{m-1}e^{jm\phi}\right) \\ &\quad + \kappa_2\left(\sum_{m=1}^{\infty} P_{m+1}e^{jm\phi} - \sum_{m=1}^{\infty} P_{m-2}e^{jm\phi}\right) \\ &= (\kappa_1+\kappa_2 e^{-j\phi})S_+(\phi) - e^{-j\phi}(\kappa_1+\kappa_2 e^{-j\phi})S_-(\phi) \\ &\quad -(\kappa_1+\kappa_2 P_1) - 2\kappa_2 e^{-j\phi} \\ &\equiv -2je^{-j\phi}\left[\frac{\kappa_1 e^{j\phi/2}+\kappa_2 e^{-j\phi/2}}{\sqrt{2(\cos\Theta-\cos\phi)}} - j\kappa_2\right] \\ &\quad -(\kappa_1+\kappa_2 P_1). \end{aligned} \tag{22'}$$

Appendix IV
Field Sum Formulas

Consider first the asymptotic E_z field sums for $(a > r > b)$ and $(r > b)$ which have, respectively, the forms:

$$S_z(r/b,\phi) = \sum_{m=1}^{\infty} e^{jm\phi}\left[\frac{\bar{x}_m}{m}\left(\frac{r}{b}\right)^m\right] - \sum_{m=3}^{\infty} e^{-jm\phi}\left[\frac{\bar{x}_{-m}}{m}\left(\frac{r}{b}\right)^m\right]$$

$$S_z(b/r,\phi) = \sum_{m=1}^{\infty} e^{jm\phi}\left[\frac{\bar{x}_m}{m}\left(\frac{b}{r}\right)^m\right] + \sum_{m=3}^{\infty} e^{-jm\phi}\left[\frac{\bar{x}_{-m}}{m}\left(\frac{b}{r}\right)^m\right].$$

Identifying the quantities

$$\lambda_+ = \lambda e^{j\phi}$$

$$\lambda_- = \lambda e^{-j\phi},$$

where $|\lambda_+| < 1$ and $|\lambda_-| < 1$, and using the definition (17') of $\bar{x}_m$, these sums have the common form

$$\begin{aligned} S_z(\lambda,\phi) &= \kappa_1\sum_{m=1}^{\infty}\frac{P_m}{m}\lambda_+^m + \kappa_1\sum_{m=1}^{\infty}\frac{P_{m+1}}{m+1}\lambda_+^m \\ &\quad -\kappa_2\sum_{m=3}^{\infty}\frac{P_{m-1}}{m-1}\lambda_-^m - \kappa_2\sum_{m=3}^{\infty}\frac{P_{m-2}}{m-2}\lambda_-^m. \end{aligned}$$

A "generic" sum is immediately recognized and evaluated. Because the generating function of the Legendre polynomials is

$$\frac{1}{\sqrt{1-2\lambda\cos\Theta+\lambda^2}} = \sum_{m=0}^{\infty} P_m\lambda^m \equiv L(\lambda), \qquad \text{for } |\lambda|<1,$$

one obtains

$$\begin{aligned} \sum_{m=1}^{\infty} P_m\frac{\lambda^m}{m} &= \int_0^{\lambda}\frac{d\xi}{\xi}\left(\sum_{m=1}^{\infty} P_m\xi^m\right) \\ &= \int_0^{\lambda}\frac{d\xi}{\xi}\left(\frac{1}{\sqrt{1-2\xi\cos\Theta+\xi^2}}-1\right) \\ &= \ln\left(\frac{2}{1-\lambda\cos\Theta+\sqrt{1-2\lambda\cos\Theta+\lambda^2}}\right) \equiv K(\lambda). \end{aligned}$$

Consequently, the desired asymptotic sum formula is

$$\begin{aligned} S_z(\lambda,\phi) &= \kappa_1 K(\lambda_+) + \kappa_2\lambda_+^{-1}[K(\lambda_+)-P_1\lambda_+] \\ &\quad -\kappa_1\lambda_-[K(\lambda_-)-P_1\lambda_-] - \kappa_2\lambda_-^2 K(\lambda_-) \\ &= (\kappa_1+\lambda_+^{-1}\kappa_2)K(\lambda_+) - \lambda_-(\kappa_1+\lambda_-\kappa_2)K(\lambda_-) \\ &\quad +(\kappa_1\lambda_-^2-\kappa_2)\cos\Theta. \end{aligned} \tag{26a}$$

The asymptotic field sums S_r and S_ϕ follow in a similar fashion using the generating function itself. In particular, the S_r sums

$$S_r(r/b,\phi) = \sum_{m=1}^{\infty}[\tilde{x}_m e^{jm\phi} + \tilde{x}_{-m}e^{-jm\phi}]\left(\frac{r}{b}\right)^m, \qquad (a<r<b)$$

$$S_r(b/r,\phi) = \sum_{m=1}^{\infty}[\tilde{x}_m e^{jm\phi} + \tilde{x}_{-m}e^{-jm\phi}]\left(\frac{b}{r}\right)^m, \qquad (r>b)$$

are encompassed by the expression:

$$\begin{aligned} S_r(\lambda,\phi) &= \kappa_1\sum_{m=1}^{\infty} P_m\lambda_+^m + \kappa_1\sum_{m=1}^{\infty}P_{m+1}\lambda_+^m \\ &\quad +\kappa_2\sum_{m=3}^{\infty} P_{m-1}\lambda_-^m + \kappa_2\sum_{m=3}^{\infty} P_{m-2}\lambda_-^m \\ &= (\kappa_1+\lambda_+^{-1}\kappa_2)L(\lambda_+) + \lambda_-(\kappa_1+\lambda_-\kappa_2)L(\lambda_-) \\ &\quad -(\kappa_1+\kappa_2\cos\Theta) - \kappa_2\lambda_+^{-1}(1-\lambda_+\lambda_-). \end{aligned} \tag{26b}$$

Similarly, the S_ϕ sums

$$S_\phi(r/b, \phi) = \sum_{m=1}^{\infty} [\tilde{x}_m e^{jm\phi} - \tilde{x}_{-m} e^{-jm\phi}] \left(\frac{r}{b}\right)^m, \quad (a<r<b)$$

$$S_\phi(b/r, \phi) = \sum_{m=1}^{\infty} [\tilde{x}_m e^{jm\phi} - \tilde{x}_{-m} e^{-jm\phi}] \left(\frac{b}{r}\right)^m, \quad (r>b)$$

are encompassed by the expression:

$$\begin{aligned} S_\phi(\lambda, \phi) &= \kappa_1 \sum_{m=1}^{\infty} P_m \lambda_+^m + \kappa_1 \sum_{m=1}^{\infty} P_{m+1} \lambda_+^m \\ &\quad - \kappa_2 \sum_{m=1}^{\infty} P_{m-1} \lambda_-^m - \kappa_2 \sum_{m=1}^{\infty} P_{m-2} \lambda_-^m \\ &= (\kappa_1 + \lambda_+^{-1} \kappa_2) L(\lambda_+) - \lambda_- (\kappa_1 + \lambda_- \kappa_2) L(\lambda_-) \\ &\quad - (\kappa_1 + \kappa_2 \cos \Theta) - \kappa_2 \lambda_+^{-1} (1 + \lambda_+ \lambda_-). \end{aligned} \quad (26c)$$

Acknowledgment

The authors would like to thank Dr. William A. Johnson for his many valuable suggestions during the initial stages of this investigation.

References

[1] R. W. Ziolkowski, "N-series problems and the coupling of electromagnetic waves to apertures: A Riemann–Hilbert approach," *SIAM J. Math. Anal.*, vol. 16, no. 2, Mar. 1985.

[2] W. A. Johnson and R. W. Ziolkowski, "The scattering of an H-polarized plane wave from an axially slotted infinite cylinder: a dual series approach," *Radio Sci.*, vol. 19, no. 1, pp. 275–291, Jan. 1984.

[3] R. W. Ziolkowski, W. A. Johnson, and K. F. Casey, "Applications of Riemann–Hilbert problem techniques to electromagnetic coupling through apertures," *Radio Sci.*, vol. 19, no. 11, Dec. 1984.

[4] T. B. A. Senior, "Electromagnetic field penetration into a cylindrical cavity," Air Force Weapons Lab. Interaction Notes, IN 221, Jan. 1975.

[5] J. N. Bombardt and L. F. Libelo, "S.E.R.A.: V. surface current, tangential aperture electric field, and back-scattering cross section for the axially slotted cylinder at normal, symmetric incidence," White Oak Lab., Silver Springs, MD, NAVSURFWPNCEN, NSWC/WOL/TR 75-39, Apr. 1975.

[6] V. N. Koshparënok and V. P. Shestopalov, "Diffraction of a plane electromagnetic wave by a circular cylinder with a longitudinal slot," *Zh. Vychisl. Mat. i Mat. Fiz.*, vol. 11, pp. 719–737, 1971; *U.S.S.R. Comp. Math. and Math. Phys.*, vol. 11, pp. 222–243, 1971.

[7] L. K. Warne, Sandia Nat. Labs., private communication.

[8] R. W. Ziolkowski and J. B. Grant, "A generalized dual series approach to the coupling of an E-polarized plane wave to a slit cylinder enclosing a concentric impedance surface," presented at Nat. Radio Sci. Meet., U.R.S.I. B-13.3, Boston, MA, June 1984.

[9] F. D. Gakhov, *Boundary Value Problems.* Elmsford, NY: Pergamon, 1966.

[10] M. H. Stone, *Linear Transformations in Hilbert Space*, Colloquim Pub., vol. 15, Am. Math. Soc., New York, 1964, ch. 4, pp. 125–154; P. M. Morse and H. Feshbach, *Methods of Theoretical Physics*, vol. 1. New York: McGraw-Hill, 1953, sec. 8.2, pp. 907–925.

[11] R. F. Harrington, *Time-Harmonic Electromagnetic Fields.* New York: McGraw-Hill, 1977.

[12] N. Marcuvitz, *Waveguide Handbook.* New York: McGraw-Hill, 1951.

[13] R. W. Ziolkowski and R. F. Schmucker, "Scattering from a slit cylinder enclosing an off-set impedance surface," presented at Nat. Radio Sci. Meet., U.R.S.I. B8-8, Boulder, CO, Jan. 1986.

[14] R. W. Ziolkowski, "Scattering from a spherical shell with a circular aperture: cross-sections and energy storage for a normally incident plane wave," presented at Nat. Radio Sci. Meet., URSI B15-4, Vancouver, BC, June 1985.

[15] R. W. Ziolkowski, D. M. Peplinski, and L. F. Libelo, "Scattering from an open spherical shell having a circular aperture and enclosing a metallic or dielectric sphere," presented at Nat. Radio Sci. Meet., U.R.S.I. B8-9, Boulder, CO, Jan. 1986.

[16] M. Abramowitz and I. A. Stegun, *Handbook of Mathematical Functions.* New York: Dover, 1965, p. 360.

[17] F. Oberhettinger, *Fourier Expansions.* New York: Academic, 1973, p. 38.

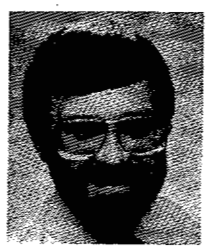

Richard W. Ziolkowski was born in Warsaw, N.Y. on November 22, 1952. He received the Sc.B. degree in physics with honors from Brown University, Providence, RI, in 1974, and the M.S. and Ph.D. degrees in physics from the University of Illinois, Urbana-Champaign, in 1975 and 1980, respectively.

He joined the Engineering Research Division at the Lawrence Livermore National Laboratory in 1981 and is currently the Engineering Modeling and Simulation Thrust Area Leader for the Electronics Engineering Department. His research interests include the application of new mathematical methods to linear and nonlinear problems dealing with the interaction of electromagnetic waves with scattering objects, plasmas, and dielectric materials.

Dr. Ziolkowski is a member of Sigma Xi, Phi Kappa Phi and the American Physical Societies.

J. Brian Grant was born in Tuscon, AZ, in 1958. He received the B.S. and M.S. degrees in electrical engineering in 1981 and 1983, respectively. He is currently pursuing a Ph.D. in Applied Physics at the College of Engineering, University of California, Davis.

In September of 1982, he joined the Lawrence Livermore National Laboratory, Livermore, CA, full time after participating in the student summer program for two years. His major responsibilities are the development of analytical and numerical tools for solving electromagnetic problems of importance to the laboratory.